CHALMERS

Adjoint-based Sensitivity Analysis for External Aerodynamics

Master's thesis in Naval Architecture and Ocean Engineering

JUNDI XU
MINGHAO LI

Department of Mechanics and Maritime Sciences
CHALMERS UNIVERSITY OF TECHNOLOGY
Göteborg, Sweden 2017

MASTER'S THESIS IN NAVAL ARCHITECTURE AND OCEAN ENGINEERING

Adjoint-based Sensitivity Analysis for External Aerodynamics

JUNDI XU
MINGHAO LI

Department of Mechanics and Maritime Sciences
Division of Marine Technology
CHALMERS UNIVERSITY OF TECHNOLOGY

Göteborg, Sweden 2017

Adjoint-based Sensitivity Analysis for External Aerodynamics
JUNDI XU
MINGHAO LI

Master's thesis X-17/390
ISSN 1652-8557
Department of Mechanics and Maritime Sciences
Division of Marine Technology
Chalmers University of Technology
SE-412 96 Göteborg
Sweden
Telephone: +46 (0)31-772 1000

Cover:
The cover shows the drag sensitivity map of Volvo XC-90 with streamlines

Chalmers Reproservice
Göteborg, Sweden 2017

Adjoint-based Sensitivity Analysis for External Aerodynamics
Master's thesis in Naval Architecture and Ocean Engineering
JUNDI XU
MINGHAO LI
Department of Mechanics and Maritime Sciences
Division of Marine Technology
Chalmers University of Technology

Abstract

In gradient-based optimisation, the adjoint method predominates the traditional methods in terms of computational cost. The adjoint method makes the gradient calculation independent of the number of design variables, which makes it an attractive choice when working with a high number of design variables.

The DrivAer model with three configurations is used in both RANS-based and DDES-based adjoint simulations. The convergence of the adjoint field is assessed by monitoring different probes with respect to the sensitivity parameter. The comparison of the sensitivity map between RANS-based and DDES-based adjoint is investigated, then the accuracy of adjoint solver prediction is assessed within its corresponding state simulations. In the current thesis, a brief procedure description of both sensitivity-based morphing and direct morphing is presented, and their merits and drawbacks are demonstrated by a series of evaluation cases. Furthermore, the DDES-base adjoint approach is applied on a realistic car model, Volvo XC90.

Keywords: Adjoint, DrivAer, aerodynamics, sensitivity map, RANS-based adjoint, DDES-based adjoint, morphing, drag force, Volvo XC90

Preface

This thesis work was performed at the Aerodynamic Group of Volvo Car Corporation R&D in Torslanda, Gothenburg from January 2017 to June 2017 and it concludes the two-year education of Master Programme in Naval Architecture and Ocean Engineering at Chalmers University of Technology. The thesis is supervised by Dr. Eysteinn Helgason and MSc. Tobias Eidevåg at VCC and finally approved by the examiner Prof. Rickard Bensow at Chalmers.

Acknowledgements

We would like to greatly thank our supervisors Eysteinn Helgason and Tobias Eidevåg at Volvo Cars, first of all for providing us this opportunity to study this interesting subject and for supporting us with any doubts both theoretically and technically throughout the thesis. We gained a lot of knowledge and could not have carried out this thesis without their encouragement and guidance.

We would also like to thank our examiner Rickard Bensow for keeping track on our thesis process and the approval of this thesis.

We are also super grateful to all the colleagues in Volvo Cars Aerodynamic Group. Thank you for creating such a comfortable working environment, which stimulates us to work in a creative and effective way. A huge thank goes for the happy lunch and fika times we shared together as well.

Last but not the least, we would like to thank Engys and ANSA support for providing quick response to our questions.

Gothenburg, August 2017

Minghao Li, Jundi Xu

Nomenclature

α	porosity distribution
β	normal node displacement
μ	dynamic viscosity
ν	kinematic viscosity
ν_t	turbulent viscosity
$\overrightarrow{D}$	direction unit vector
$\overrightarrow{S}$	surface normal vector
ρ	air density
τ_w	wall shear stress
$\mathbf{u}$	adjoint velocity
$\mathbf{v}$	primal velocity
$\tilde{d}$	length scale
ε	dissipation
A	projected front area
ATC	**A**djoint **T**ranspose **C**onvection
C_d	drag coefficient
C_dA	drag factor
C_p	pressure coefficient
$D(\mathbf{v})$	rate of strain tensor
$DDES$	**D**elayed **D**etached **E**ddy **S**imulation
DES	**D**etached **E**ddy **S**imulation
F_d	drag force
f_d	damping function
FDM	**F**inite **D**ifference **M**ethods
J	objective function
k	kinetic energy
LES	**L**arge **E**ddy **S**imulation
MRF	**M**oving **R**eference **F**rame
$NACA$	**N**ational **A**dvisory **C**ommittee on **A**eronautics (USA)
$OpenFOAM$	**O**pen source **F**ield **O**peration **A**nd **M**anipulation
p	primal pressure
p_∞	free-stream static pressure
P_b	production of turbulence kinetic energy (buoyancy)
P_k	production of turbulence kinetic energy (mean velocity gradients)

p_{tot} total pressure

q adjoint pressure

$RANS$ **R**eynolds-**A**veraged **N**avier–**S**tokes equations

$URANS$ **U**nsteady **R**eynolds-**A**veraged **N**avier–**S**tokes equations

V_∞ free-stream speed

List of Figures

Contents

1 Introduction

This chapter provides a brief introduction to the thesis background, its purpose and limitations.

1.1 Background

The aerodynamic properties of passenger cars have a significant impact on the car performance in terms of comfort, safety and economics.

The aerodynamic optimisation is normally performed by gradient-based optimisation methods. The gradient-based optimisation algorithms generally include an objective function with respect to the flow and design variables and the underlying principle is to calculate the gradients or sensitivities of the objective function w.r.t. the design variables. When applying the traditional methods, for example, the Finite Difference Method, the computational burden increases dramatically with an increasing number of design variables. This is because the finite difference method first requires one simulation for the original objective function and each new objective function with one design variable modification requires another simulation. Supposing that there are N design variables, N+1 simulations are needed to obtain the sensitivities. For an industrial vehicle geometry, N could be over several millions, which makes the computational cost unaffordable.

An alternative method, the adjoint method, is much more efficient for gradient-based optimisation with a large number of design variables. It has been a long history of the application of the adjoint techniques in CFD optimisation problems and several remarkable works regarding aerodynamic shape optimisation can be found in [1, 2, 3, 4, 5, 6, 7]. The advantage of the adjoint method is that it only involves two simulations independent of the number of design variables. One is the conventional CFD simulation for flow velocity and pressure field and another is the adjoint simulation for adjoint field solutions in which the sensitivities of the objective function with respect to the design variables are obtained. For the objective of reducing aerodynamic drag, the design variables could be each surface cell on the vehicle and the so-called 'sensitivity maps' showing the gradient information at every surface mesh location can be obtained from two simulations. Obviously, the adjoint method excels the traditional methods with lower computational effort and higher efficiency.

1.2 Purpose

The aim of this thesis is to apply and evaluate the adjoint method for aerodynamic drag optimisation. Both the RANS-based and DDES-based adjoint simulations for the generic DrivAer model will be conducted, in order to figure out the difference of flow features and sensitivity maps between these two states. To evaluate to what extent one can trust the sensitivity map, several potential regions will be selected to validate the trends of the sensitivity map. The validation flow will be that one first morphs the geometry based on the sensitivity map, followed by a re-simulations of the morphed geometry to see if there is any drag reduction. Furthermore, Volvo Cars provides a detailed Volvo XC90 model and they are interested in the performance of using the adjoint method for a complex industrial car. The DDES-based adjoint simulations then will be performed for the XC90 model as well.

1.3 Limitations

The limitations are first of all only four potential regions are used to evaluate the trends of the sensitivity maps. Another limitation is the lack of experimental data, which makes it difficult to conclude the sensitivity result of which state is more accurate and reliable.

2 Theory

This chapter presents the theory behind the adjoint methodology for both steady state and transient simulations together with the objective function and definition of several relevant parameters.

2.1 Adjoint methodology

The adjoint method has long been considered an efficient tool for gradient-based optimisation because it only consists of two simulations, i.e. primal and adjoint simulations, regardless of the number of design variables [8]. The primal flow simulation provides the normal solution fields, i.e. velocity, pressure and turbulence quantities. Inputting the primal fields into the adjoint equations, the so-called adjoint velocity and pressure will be calculated. Then one obtains the gradient-based sensitivities which are formulated in terms of primal and adjoint fields.

The primal and adjoint equations (Eqn. 2.1 - 2.4) for steady state incompressible flow are:

$$\underbrace{(\mathbf{v}\cdot\nabla)\mathbf{v}}_{\text{convection}} = \underbrace{-\nabla p}_{\text{pressure}} + \underbrace{\nabla\cdot(2\nu D(\mathbf{v}))}_{\text{diffusion}} \tag{2.1}$$

$$\nabla\cdot\mathbf{v} = 0 \tag{2.2}$$

where $\mathbf{v}$, p and ν are primal velocity, pressure and kinematic viscosity, while D($\mathbf{v}$) represents the rate of strain tensor.

$$\underbrace{-(\mathbf{v}\cdot\nabla)\mathbf{u}}_{\text{backward convection}} + \underbrace{-\nabla\cdot\mathbf{uv}}_{\text{transpose convection}} = \underbrace{-\nabla q}_{\text{adjoint pressure}} + \underbrace{\nabla\cdot(2\nu D(\mathbf{u}))}_{\text{adjoint diffusion}} \tag{2.3}$$

$$\nabla\cdot\mathbf{u} = 0 \tag{2.4}$$

where $\mathbf{u}$ and q represent adjoint velocity and adjoint pressure respectively.

Comparing the primal and adjoint equation systems, several similarities are observed including pressure and diffusion terms. The adjoint convection term differs from the primal standard convection by decomposing it into a backward convection term and a transpose convection term. The backward convection term indicates how information about the flow is transported from downstream to upstream. The adjoint transpose convection (ATC) introduces a high degree of cross-coupling among the three components of the adjoint velocity, which makes it difficult to be implemented implicitly in a segregated algorithm. For industrial auto-generated computational grid, the ATC term is the main potential source of adjoint solver instability and therefore special treatments such as using limiters or damping functions must be employed [3].

The adjoint solver is categorised into continuous and discrete adjoint depending on how the adjoint equations are derived. The continuous adjoint differentiates the partial differential equations, in this case, the Navier-Stokes equations, prior to the discretisation while the discrete adjoint starts by discretising the partial differential equations and then these equations are differentiated. A detailed comparison of these two approaches is presented in [3].

By solving both primal and adjoint equation systems using the continuous approach, the surface shape sensitivities w.r.t. an objective function J can be computed from Eqn. 2.5.

$$\frac{\partial J}{\partial \beta} = \frac{\partial \mathbf{v}}{\partial \mathrm{n}}\cdot\frac{\partial \mathbf{u}}{\partial \mathrm{n}} \tag{2.5}$$

where β stands for cell normal displacement.

The objective in the current thesis is to reduce the drag force using surface shape sensitivities. The magnitude of the sensitivities represents the gradient of the drag function with respect to the local normal displacement, and the sign indicates the surface cell moving direction to reduce the drag force.

2.2 Primal field

In the thesis, two turbulence modelling approaches are applied to calculate the primal flow field which is used as an input to the adjoint simulation, i.e. RANS approach for steady state and DDES for transient. A brief description of these two approaches and the turbulence modelling will be presented in this section.

2.2.1 Steady state

In Reynolds-averaged Navier-Stokes (RANS) equations, the instantaneous variable is decomposed into a mean and a fluctuating quantity as:

$$v_i = \bar{v}_i + v_i', \ p = \bar{p} + p' \tag{2.6}$$

The steady state RANS equations consist of the time averaged continuity equation and the Navier-Stokes equation.

$$\frac{\partial \bar{v}_i}{\partial x_i} = 0 \tag{2.7}$$

$$\rho \frac{\partial \bar{v}_i \bar{v}_j}{\partial x_j} = -\frac{\partial \bar{p}}{\partial x_i} + \frac{\partial}{\partial x_j}\Big(\mu \frac{\partial \bar{v}_i}{\partial x_j} - \rho \overline{v_i' v_j'}\Big) \tag{2.8}$$

To close the RANS equations system, the nonlinear Reynolds stress term ($\rho \overline{v_i' v_j'}$) requires additional modelling. Therefore, various RANS-based turbulence models are developed, such as Realizable k-ε model, k-ω model, Spalart-Allmaras model etc. The computational cost of this type of modelling is quite cheap since the RANS approach only calculates the mean values. In the current thesis, RKE model with RANS approach is applied for steady state simulations.

2.2.2 Transient

Although RANS approach is able to well simulate the mean flow field with relatively low computational cost, the accuracy of the prediction in massive separation regions, such as the vehicle wake region, is not sufficient [9]. Alternatively, the Detached Eddy Simulation (DES) which is a mixture of LES and URANS is introduced to capture the characteristics of various eddy scales with economical cost.

DES

Generally, Large Eddy Simulation (LES) is more capable to solve the flow features, for example the wake flow, than RANS. However, LES has a demanding requirement on the mesh resolutions particularly in the near-wall regions, which considerably increases the computational burden. As an alternative, Unsteady RANS (URANS) model arises to make an accurate prediction of wall-bounded flow with fairly coarse mesh. In URANS, the Reynolds decomposition law is employed as:

$$\bar{v}(t) = \frac{1}{2T}\int_{t-T}^{t+T} v(t)dt, \ v = \bar{v} + v'' \tag{2.9}$$

The URANS equations are:

$$\frac{\partial \bar{v}_i}{\partial x_i} = 0 \tag{2.10}$$

$$\rho \frac{\partial \bar{v}_i}{\partial t} + \rho \frac{\partial \bar{v}_i \bar{v}_j}{\partial x_j} = -\frac{\partial \bar{p}}{\partial x_i} + \frac{\partial}{\partial x_j}\Big(\mu \frac{\partial \bar{v}_i}{\partial x_j} - \rho \overline{v_i' v_j'}\Big) \tag{2.11}$$

The objective of DES approach is to eliminate the requirement of high mesh resolution in wall-parallel planes. The low-Re number RANS turbulence model is applied in the near-wall region (the URANS region), and for the outer region, LES is used to capture the detached eddies [9], see Figure 2.1.

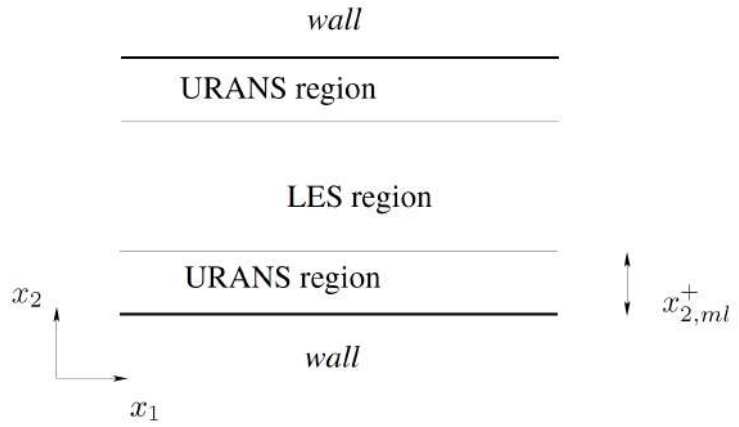

Figure 2.1: *The URANS and LES regions in DES [9]*

DES can be regarded as a hybrid LES-RANS, where the turbulent RANS viscosity is used in the URANS region and the turbulent subgrid-scale (SGS) viscosity is used in the LES region[9].

DDES

DES is designed to treat the boundary layer using URANS model and the separation region with LES model, but in spite of that, it cannot have correct performance in thick boundary layers and shallow separation regions due to its formulation. This occurs when the grid spacing parallel to the wall $\Delta_{||}$ becomes less than the boundary layer thickness δ[10], it may trigger too early detachment[11].

To deal with this unexpected phenomena, Delayed Detached-Eddy Simulation (DDES)[10] is introduced, where the boundary layer is shielded with a damping function f_d[10](the subscript "d" stands for "delayed") which is applied to protect the boundary layer against LES content. Therefore, Delayed Detached-Eddy Simulation (DDES) is less prone to the so-called "grey area problem", which could prevent from triggering too early detachment[11]. In the current thesis, SA model with DDES approach (SA-DDES) is applied for the transient primal flow.

According to Spalart et al [12], the Spalart-Allmaras model in DES can be written as Eqn.2.17. The length scale $\tilde{d}$ controls the eddy viscosity:

$$\tilde{d} = \min(d, C_{DES}\Delta) \tag{2.12}$$

where d is equal to the distance to the nearest wall, C_{DES} is usually set to 0.65 and $\Delta = \max(\Delta x, \Delta y, \Delta z)$.

After inserting the damping function f_d into Eqn.2.12, $\tilde{d}$ is re-defined as:

$$\tilde{d} \equiv d - f_d \max(0, d - C_{DES}\Delta) \tag{2.13}$$

For DDES, in order to apply to an eddy-viscosity model, the parameter r (Eqn. 2.18) in Spalart-Allmaras model is modified as r_d which is more robust in irrotational regions. In the logarithmic region, the parameter r_d equals to 1 and down to 0 gradually closing to the edge to boundary layer. The kinematic viscosity ν in the numerator corrects the near-wall performance by ensuring that r_d remains away from 0.

$$r_d \equiv \frac{\nu_t + \nu}{\sqrt{U_{i,j}U_{i,j}}\kappa^2 d^2} \tag{2.14}$$

The damping f_d is designed to be 1 in the LES region where $r_d \ll 1$, and 0 elsewhere. f_d defined as[10]:

$$f_d \equiv 1 - tanh([8r_d]^3),$$

2.2.3 Turbulence model

Turbulence model plays a key role when performing the adjoint simulations, since the accuracy of adjoint method depends significantly on the primal flow. Therefore the prediction of turbulence features in the primal field, such as boundary layer separation around the rear trunk and the resulted detached-eddies, will influence the accuracy of the adjoint solution. Two turbulence modelling approaches are applied in the current thesis: Realizable k-ε model with RANS approach (RKE-RANS)[13] and Spalart-Allmaras model[12] together with Delayed Detached-Eddy approach (SA-DDES).

Realizable k-ε model

Realizable k-ε (RKE) model includes two transport equations to represent the turbulent properties of the flow, which allows the model naturally to take the history effects from convection and diffusion of turbulent energy into account. The formulations are independent of the flow topology which makes them suitable to simulate complex geometries, therefore it has become a common turbulence model for the automotive industry.

Compared with the standard k-ε model, the Realizable k-ε model improves the equation for ε (Eqn. 2.16), and uses a variable C_μ instead of the constant results. The improvement contributes to a better performance for flows involving rotation and recirculation with strong streamline curvature and separation. The transport equations are given by:

$$\frac{\partial}{\partial t}(\rho k) + \frac{\partial}{\partial x_j}(\rho k u_j) = \frac{\partial}{\partial x_j}\Big[\Big(\mu + \frac{\mu_t}{\sigma_k}\Big)\frac{\partial k}{\partial x_j}\Big] + P_k + P_b - \rho\varepsilon - Y_M + S_k \tag{2.15}$$

$$\frac{\partial}{\partial t}(\rho \varepsilon) + \frac{\partial}{\partial x_j}(\rho \varepsilon u_j) = \underbrace{\frac{\partial}{\partial x_j}\Big[\Big(\mu + \frac{\mu_t}{\sigma_\varepsilon}\Big)\frac{\partial \varepsilon}{\partial x_j}\Big]}_{\text{Diffusion}} + \underbrace{\rho C_1 S \varepsilon}_{\text{Generation}} - \underbrace{\rho C_2 \frac{\varepsilon^2}{k + \sqrt{\nu\varepsilon}}}_{\text{Destruction}} + \underbrace{C_{1\varepsilon}\frac{\varepsilon}{k} C_{3\varepsilon} P_b}_{\text{Buoyancy}} + S_\varepsilon \tag{2.16}$$

where

$$C_1 = \max\big[0.43, \frac{\eta}{\eta + 5}\big],\ \eta = S\frac{k}{\varepsilon},\ S = \sqrt{2 S_{ij} S_{ij}}$$

$$\mu_t = \rho C_\mu \frac{k^2}{\varepsilon},\ \text{with } C_\mu = \frac{1}{A_0 + A_s \frac{kU*}{\varepsilon}}$$

In these equations, P_k and P_b represent the generation of turbulence kinetic energy due to the mean velocity gradients and buoyancy respectively and both are calculated in the same way as standard k-ε model.

The main problem of this model is the wall treatment issue, as its wall function only works well when y^+ ($y^+ = u_* y/\nu$) is over 20 which is a precondition to predict the accurate primal field. Therefore, the first cell height setting needs more attention in the mesh generation to ensure the requirements of using wall function could be fulfilled.

Spalart-Allmaras model

The Spalart-Allmaras (SA) model is a one-equation model which solves a transport equation model for a viscosity-like variable, $\tilde{\nu}$. It seems to be a good comprise between algebraic models and two equation models because it neither needs to express directly the eddy viscosity nor the turbulent eddy viscosity in the near-wall layer with wall functions.

The transport equation for variable $\tilde{\nu}$ is given by [12]:

$$\frac{\partial \tilde{\nu}}{\partial t} + u_j \frac{\partial \tilde{\nu}}{\partial x_j} = \underbrace{C_{b1}\Big[1 - f_{t2}\Big]\tilde{S}\tilde{\nu}}_{\text{Production}} + \underbrace{\frac{1}{\sigma}\Big[\nabla \cdot \big[(\nu + \tilde{\nu})\big] + C_{b2}|\nabla\tilde{\nu}|^2\Big]}_{\text{Diffusion}} - \underbrace{\Big[C_{w1} f_w - \frac{C_{b1}}{\kappa^2} f_{t2}\Big]\Big(\frac{\tilde{\nu}}{d}\Big)^2 + f_{t1}\Delta U^2}_{\text{Destruction}} \tag{2.17}$$

In order to ensure that ν equals to $\kappa y u_\tau$ in the boundary layer, the damping function f_{v1} is introduced, then the turbulent eddy viscosity is written as:

$$\nu_t = \tilde{\nu} f_{v1}, \text{ where } f_{v1} = \frac{\chi^3}{\chi^3 + C_{v1}^3}, \text{ with } \chi = \frac{\tilde{v}}{v}$$

The vorticity magnitude S is modified so that $\tilde{S}$ maintains its log-layer behaviour:

$$\tilde{S} \equiv S + \frac{\tilde{\nu}}{\kappa^2 d^2} f_{v2}$$

To accelerate the decaying of destruction in the outer region of the boundary layer, the function f_w is defined as:

$$f_w(g) = g\left(\frac{1 + c_{w3}^6}{g^6 + c_{w3}^6}\right)^{1/6}, \text{ with } g = r + c_{w2}\left(r^6 - r\right), \; r = \frac{\tilde{\nu}}{\tilde{S}\kappa^2 d^2} \tag{2.18}$$

More detailed information can be found in [14] and [12].

2.3 Adjoint field

The surface sensitivity is calculated with a segregated approach. This segregated approach is to use a fixed static primal as input to the adjoint equations, which is simple and computationally cheap. Since the primal field is only solved once, any error in the input will be carried on throughout the adjoint solution, leading to inaccuracy and increasing the possibility of divergence. Therefore, a fully converged primal field is required prior to the start of the adjoint solution.

All the RANS-based and DDES-based adjoint equations are solved under the frozen turbulence assumption, which assumes that the derivatives of all turbulence quantities with respect to the design variables are negligible. The benefit of using this assumption is that no adjoint turbulence equations are solved, which makes the equation system simpler. Although resolving the adjoint turbulence equation would improve the accuracy of the sensitivity map, some previous works[15] show that the qualitative trends will not be impacted, especially for the sign of sensitivities.

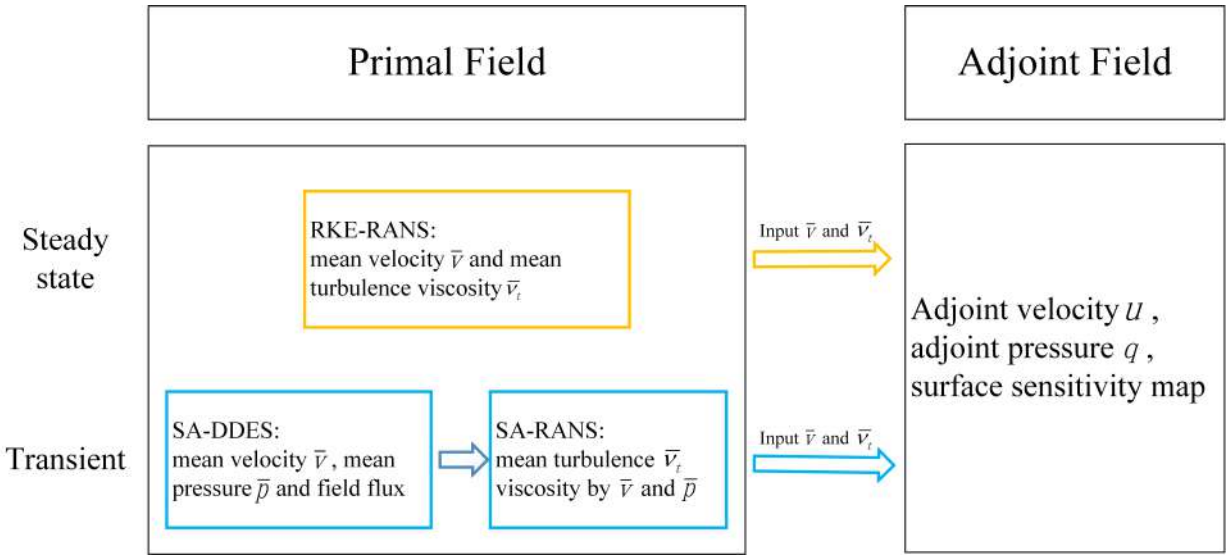

Figure 2.2: *Adjoint simulation procedure for steady state and transient*

In the RANS-based adjoint simulations, the input is the fully converged primal results including velocity, flux and turbulence viscosity. For the DDES-based adjoint simulations, the time-averaged fields will be taken as

an input. However, due to that the corresponding time-averaged turbulence viscosity ν_t from DDES only represents the LES quantity rather than the whole domain, it needs to be recalculated with time-averaged velocity and pressure via the Spalart-Allmaras RANS model[15]. Figure 2.2 illustrates the procedure for both steady state and the transient adjoint simulations.

2.4 Drag force objective

The vehicle aerodynamic drag force mainly consists of form drag which is also called pressure drag that arises because of the uneven pressure distribution on the vehicle, and skin friction drag due to the viscous shear effect. The total drag force on the objective surfaces in the flow direction is calculated from Eqn. 2.19.

$$F_d = \sum_S (p_{static} \cdot d\overrightarrow{S} + \tau_w \cdot d\overrightarrow{S}) \cdot \overrightarrow{D} \tag{2.19}$$

where p_{static} is the static pressure, $\overrightarrow{S}$ is the surface normal vector, τ_w is the wall shear stress and $\overrightarrow{D}$ is the direction unit vector.

To make the drag force dimensionless, the drag factor (C_dA) is introduced and defined as Eqn. 2.20. This is a commonly used quantity of rating a car's aerodynamic performance.

$$C_dA = 2F_d/\rho u^2 \tag{2.20}$$

where F_d is the drag force, ρ is the density of the fluid, u is the flow speed and A is the frontal area.

The pressure coefficient C_p and total pressure p_{tot} are defined as:

$$C_p = \frac{p - p_\infty}{\frac{1}{2}\rho V_\infty^2} = \frac{p_{static}}{\frac{1}{2}\rho V_\infty^2} = \frac{\text{local pressure} - \text{free-stream static pressure}}{\text{free-stream dynamic pressure}} \tag{2.21}$$

$$p_{tot} = p_{static} + \frac{1}{2}\rho V_\infty^2 \tag{2.22}$$

where V_∞ is the free-stream speed.

3 Methodology

The procedure for the CFD simulations including geometry configurations, computational domain and grid, solving and post-processing is described in this chapter. The simulations are performed using ELEMENTS and the geometry preparation and morphing is done using ANSA. Two methods are used to morph the geometries which are shape sensitivity morphing and direct morphing.

3.1 Geometry

The DrivAer model is a generic car model developed at the Institute of Aerodynamics and Fluid Mechanics of the Technische Universität München (TUM), in cooperation with Audi and BMW [16]. The aim is to close the gap between strongly simplified models such as the Ahmed body and highly complex production cars and thus boost the passenger vehicle aerodynamic research and development. The model contains several geometry variants, for example the three rear back configurations used in this thesis: fastback, notchback and squareback (Figure 3.1).

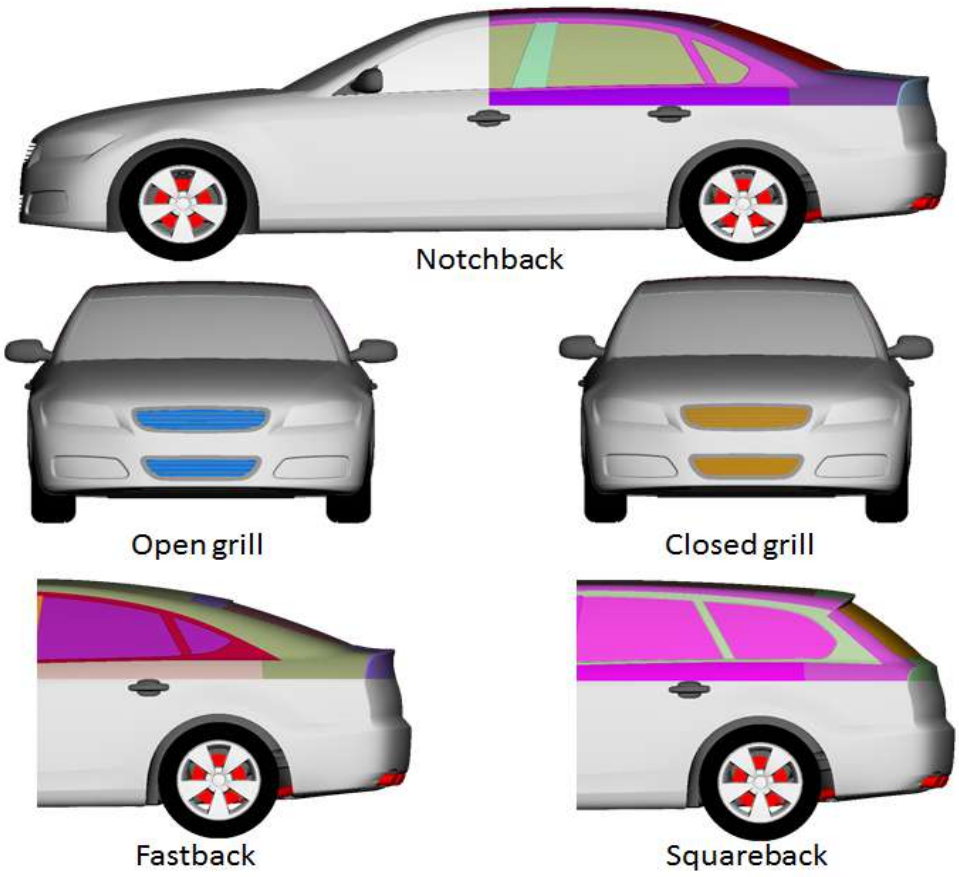

Figure 3.1: *DrivAer model configurations*

In this thesis, all the three back configurations were investigated using both steady state and transient simulations, but the main concentration is on the notchback. The notchback configuration is then subdivided into a closed grill geometry which is tested in the beginning stage and an open grill standard geometry for detailed analysis. The surface sensitivities based morphing was applied to the standard open grill notchback geometry to validate the trends of the sensitivity maps.

3.2 Computational domain and boundary conditions

A sufficiently large virtual wind tunnel is chosen as the computational domain for all model configurations as shown in Figure 3.2. The car model is located 25m behind the inlet and 75m before the outlet. There are several refinement zones around the car with finer grid, including six boxes with increasing refinement levels, an underbody wake box and a rear wake zone.

The inlet boundary condition is imposed with a freestream velocity of $38.89\,\mathrm{m\,s^{-1}}$ ($140\,\mathrm{km\,h^{-1}}$) and the various turbulent quantities (e.g. k, ε, $\tilde{\nu}$) at the inlet are defined using a turbulent mixing length of 0.01 m and intensity of 1% in the appropriate formulas. The outlet is prescribed as a pressure outlet boundary condition. To model the rotating wheels, a moving wall condition is imposed on the vehicle wheels as well as on the domain floor. The rest of the domain boundaries, both sides and top patches, are prescribed as slip wall conditions while the vehicle exterior has no-slip wall boundaries.

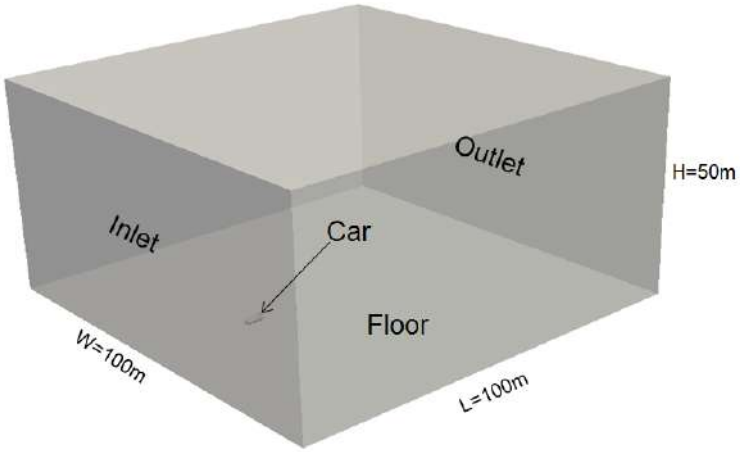

Figure 3.2: *Computational domain*

3.3 Computational grid

The mesh generation is performed using an enhanced version of the OpenFOAM utility *snappyHexMesh*. The computational grid consists of hexahedral and split-hexahedral elements. The methodology behind *snappyHexMesh* is found in [17].

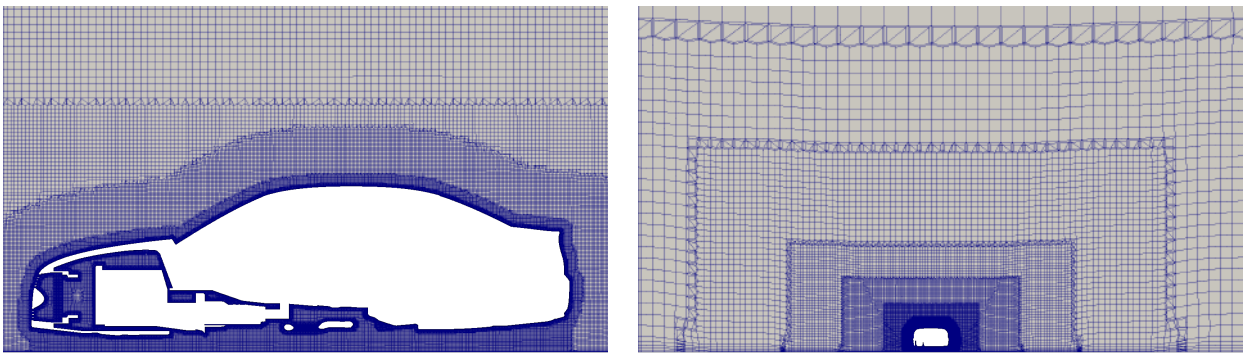

Figure 3.3: *Computational grid for notchback configuration*

The computational grid setting depends on the choice of turbulence model. Two types of mesh settings are defined for Spalart-Allmaras (SA) and Realizable k-ε (RKE) model respectively in order to fulfil the requirement of using wall functions. A relatively coarse mesh with larger first cell height is set for RKE mesh to ensure that

the y^+ value is sufficiently large (i.e. $y^+ > 20$) to apply wall functions. No grid size limitation arises from y^+ for the SA model as a hybrid wall treatment is applied. Therefore a smaller base mesh size is used and more layers are added in order to solve the flow more accurately. The cell counts range from 48 million cells to 93 million cells. The computational grid and refinement regions for notchback open grill configuration is shown in Figure 3.3.

3.4 Solving

This section describes the primal and adjoint solver setup including the choice of solver, the discretisation schemes, solver stability and time steps etc.

3.4.1 Primal solver setup

The *simpleFoam* and *pisoFoam* solvers are used for steady state RANS primal calculation and transient DDES primal calculation respectively. The Spalart-Allmaras tubulence model is applied to close the transient equation system while the Realizable k-ε model is selected for the RANS primal solver. The SA model is also tested for the steady state simulation. However, a high fluctuation of up to 20 C_dA counts was observed.

Each steady state simulation applies a 2nd order scheme to discretise the momentum and turbulence equations. For transient solutions, a blended scheme is used for the velocity convective term. The robust hybrid scheme contributes to a high level of accuracy and stability for DES/LES type calculations. The schemes of turbulence fields for transient are identical to steady state choices.

In terms of time step, the steady state simulations run 15000 iterations which is considered sufficiently long to ensure a fully converged primal result. As tiny fluctuation still exists, the last 1000 iterations are averaged. The above efforts aim to achieve a stable adjoint input to minimise the influence of any error from the primal result.

The transient primal field is averaged for 3s after an initial flushing of the computational domain. A detailed analysis of the averaging period effect on the surface sensitivity map is found in [18]. For DrivAer model, this 3s average time is long enough to ensure a decent surface sensitivity map that indicates the trend of the deformation direction.

3.4.2 Adjoint solver setup

The *helyxAdjoint* solver provided by ELEMENTS is used for the adjoint simulations. The continuous adjoint equations are solved with traditional segregated SIMPLE algorithm.

A 2nd order scheme for the adjoint velocity discretisation is applied to get a consistent accuracy order with primal solutions. While the induced stability issue, in particular originating from the ATC term as discussed in Section 2.1, requires special treatments.

The simplest way is to add an adjoint velocity limiter that suppresses or even clips bad cells with extreme values. A more complex but versatile method applied here is to use a dynamic masking function which damps the contribution from the ATC term.

For the DDES-based adjoint simulation, the turbulence viscosity is recalculated via Spalart-Allmaras RANS model. The SA iterations thus impacts the adjoint sensitivities. Considering the complexity of the vehicle geometry and the cheap computational cost of this quantity, a total of 10000 SA iterations are used in order to guarantee the convergence. Figure 3.4 illustrates the influence from the number of SA iterations on the adjoint sensitivity map for the fastback configuration.

Figure 3.4: *Comparison of sensitivity map for various SA iterations in DDES-based adjoint for fastback configuration*

3.5 Morphing

To validate the trends of the surface sensitivity map, a geometry morphing based on the sensitivity field is done. How to perform a good morphing to reflect the sensitivity map prediction is of vital importance. Two approaches, namely shape sensitivity morphing and direct morphing, will be discussed in this section. Both morphing approaches are applied using the software ANSA.

3.5.1 Shape sensitivity morphing

The shape sensitivity morphing is performed by reading the sensitivity results obtained from OpenFOAM and morphing the geometry in ANSA. One advantage of this approach is that it allows the visualisation of sensitivities by means of contour plots and several pre-processing functions are available to produce a set of smoothed sensitivities.

In order to obtain a smooth surface after morphing, the sensitivities need to be pre-treated with neighbour based smoothing. Firstly, the high or low peaks in the sensitivity values are flattened depending on the user defined maximum and minimum threshold values. Next, the smoothing is operated according to the specified number of smoothing zones and iterations. Basically, the smoothing algorithm detects the areas where significant changes in sensitivity exists and then smooths them in order to avoid noises. Figure 3.5 shows how the sensitivity map changes with respect to different smoothing parameter settings.

In addition, the sensitivity-based displacement contour can be saved as an ASCII file after pre-processing if required. These saved displacement vectors are quite convenient for making a series of morphing by various displacement magnitude specifications. Several transformation options such as translation, rotation and symmetry are also available to modify the sensitivity field in a high degree of flexibility. The symmetry transformation is used to mirror one side of the displacement vectors to the other side so that a symmetric geometry morphing is guaranteed.

When morphing the geometry with the pre-processed sensitivity map, the deformation entities and bounds need to be specified. The bounds control the boundary of the allowed geometry deformation region. The region inside the bounds is allowed to deform based on the surface sensitivities. Example showing the application of two deformation entities and bounds selection is shown in Figure 3.6. The first option with bounds selection (the blue dense lines) identical to the investigation region only deforms the selected region, but a sharp edge around the boundaries may exist. The latter option with bounds selection larger than the investigation region deform both the selected region and its vicinity, which makes the surface smoother than that in the first option.

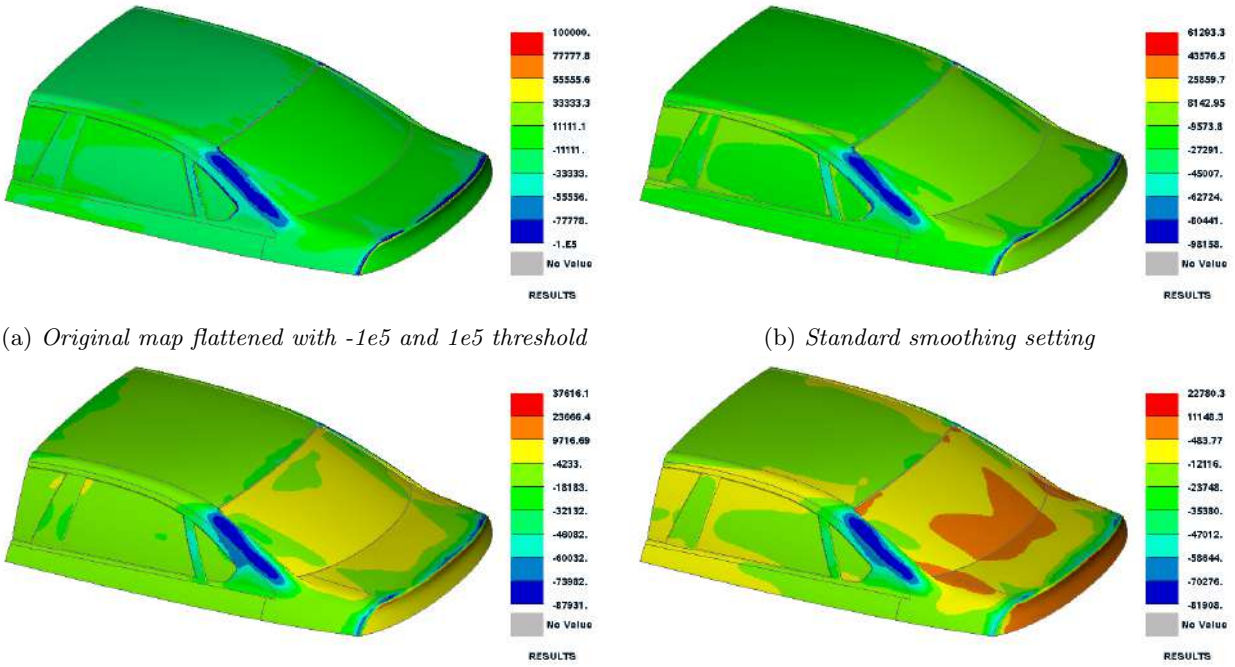

(a) *Original map flattened with -1e5 and 1e5 threshold*

(b) *Standard smoothing setting*

(c) *Large smoothing setting*

(d) *Over smoothing setting*

Figure 3.5: *Sensitivity map smoothing with different settings*

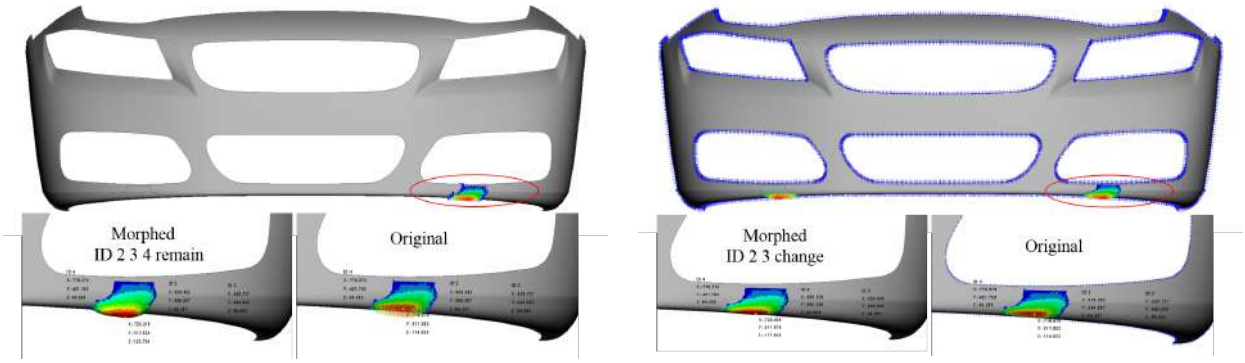

(a) *Exact deformation entities and exact bounds*

(b) *Larger deformation entities and larger bounds*

Figure 3.6: *Comparison of different deformation entities and bounds selection*

3.5.2 Direct morphing

Direct morphing can easily result in a smoother surface compared to shape sensitivity morphing. One method is to define morphing boxes to control the morphing regions [19]. Another method applied here is the Direct Fitting Movement (DFM) function. The direct morphing is performed using the geometry surfaces. One disadvantage is that the sampled sensitivity filed is unable to be mapped onto the CAD files in ANSA. Due to the absence of this tangible link between the geometry and the sensitivity field, the direct morphing has a large freedom depending on the engineers' experience and interpretation of the sensitivity map.

Take the rear trunk region as an example, the spoiler region is divided into 3 pieces and the most important regions are the upper and lower pieces, seen in Figure 3.7a. The DFM function will be defined in both pieces, which means the *control entities*, *translate vector*, *morphed entities* and *bounds* will be specified. In Figure 3.7c, the light green part is selected as *control entities* which will be translated as a rigid area; the yellow arrow is the *translate vector* which defines the translation direction; the purple region is the *morphed entities* which are

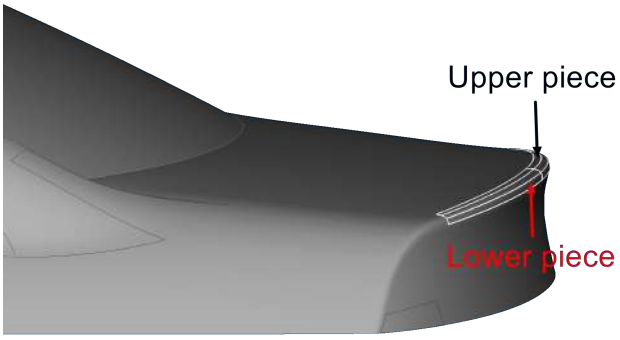

(a) *Three pieces in spoiler region*

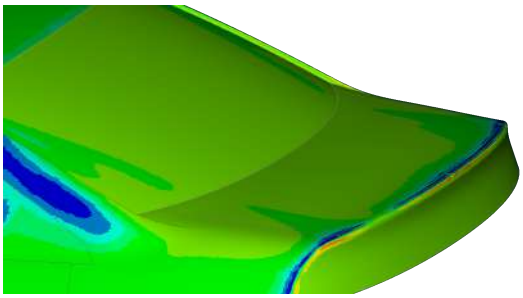

(b) *Sensitivity map in spoiler region*

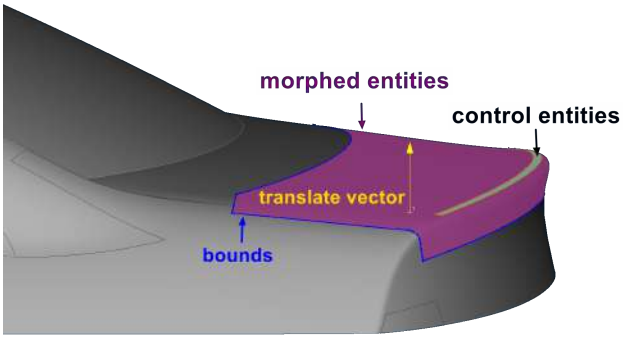

(c) *Morphing definition of the upper piece*

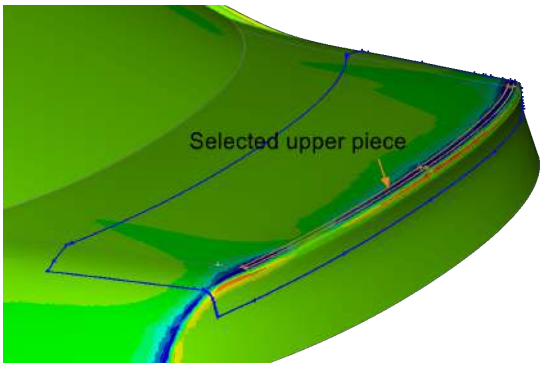

(d) *Sensitivity map for the upper piece*

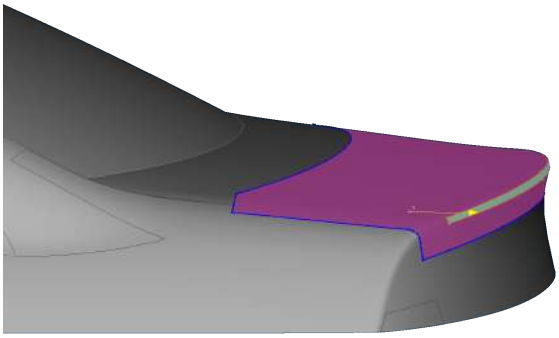

(e) *Morphing definition of the lower piece*

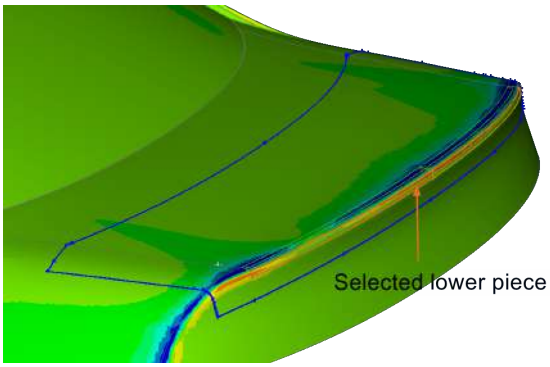

(f) *Sensitivity map for the lower piece*

Figure 3.7: *Sensitivity map with direct morphing region selection*

permitted to be affected by the translation of the *control entities*; and the blue line around it is the *bounds* that define the restriction for the edges, i.e. the geometry modification is only performed within this blue line. DFM function offers a high flexibility to operate a series of morphing with various displacements.

The DFM functions control the same morphing entities and bounds, refer to the purple area and blue line in Figure 3.7c, 3.7e. In order to morph the geometry more precisely, the sensitivities could be mapped on the geometry with some node values missing, hence the engineer could visualise the most sensitive regions. Figure 3.7b shows the variation of sensitivities on the edge of the trunk lid, and the upper piece concentrates on the blue region and the lower piece on the red region, seen in Figure 3.7d, 3.7f. Additionally, more pieces could be split into *control entities* and each piece can be appointed with the respective *translate vector* and displacements to make the geometry morphing reflects the sensitivity map prediction more accurately. After the displacement specification, the selected *morphed entities* will be smoothly morphed.

4 Analysis of the DrivAer model

The steady state and transient simulations of all the DrivAer model configurations will be elaborated in this chapter. The primal and adjoint field in each configuration will be analysed. The main focus is on the notchback open grill configuration on which the trends of the sensitivity map are validated by the selected regions on the geometry. The fastback and notchback configurations only run the steady state and transient simulations to obtain the sensitivity maps and no geometry morphing is done.

4.1 Notchback closed grill configuration

As a starting point, the notchback closed grill configuration was simulated. By closing the front, the air is restricted to only flow around the vehicle exterior without going through engine bay area, which in consequence eliminates the disturbance from them and yields a simplified simulation.

The primal flow convergence is checked in the first stage by means of residual, probes and the target drag factor C_dA plots. The steady state and transient simulations provide similar C_dA results: 0.565 and 0.564 respectively. Comparing to the PVT wind tunnel experimental data 0.549 [20], roughly 0.015 C_dA over prediction is observed. There is minor difference between these geometries, mainly the rims and tires which can contribute to some of the difference here. For the adjoint field convergence, the probe plots of sensitivity field (G-fdrag) and the volume report plots of adjoint velocity (Ua-fdrag) are monitored and approximately 10000 iterations are required for both states.

The surface sensitivities for drag minimisation from the RANS-based and the DDES-based adjoint simulations are shown in Figure 4.1. The blue region wants to move inwards and the red region outwards to reduce drag. The sensitivity map does not indicates how big the displacement should be, but only how sensitive the total drag is to the normal motion of the surface. The RANS-based adjoint produces a fairly symmetric sensitivity field for both the exterior and underbody. The slight asymmetry of the sensitivity field on the rear part of the vehicle is caused by the asymmetrical underbody, the exhaust system for example. For the largest part of the vehicle exterior, the DDES-based adjoint provides similar sensitivity distributions. Difference is observed in the front part of the underbody, in particular the area around the front wheelhouse where the DDES-based adjoint predicts an inward blue rather than an outward red in RANS-based adjoint.

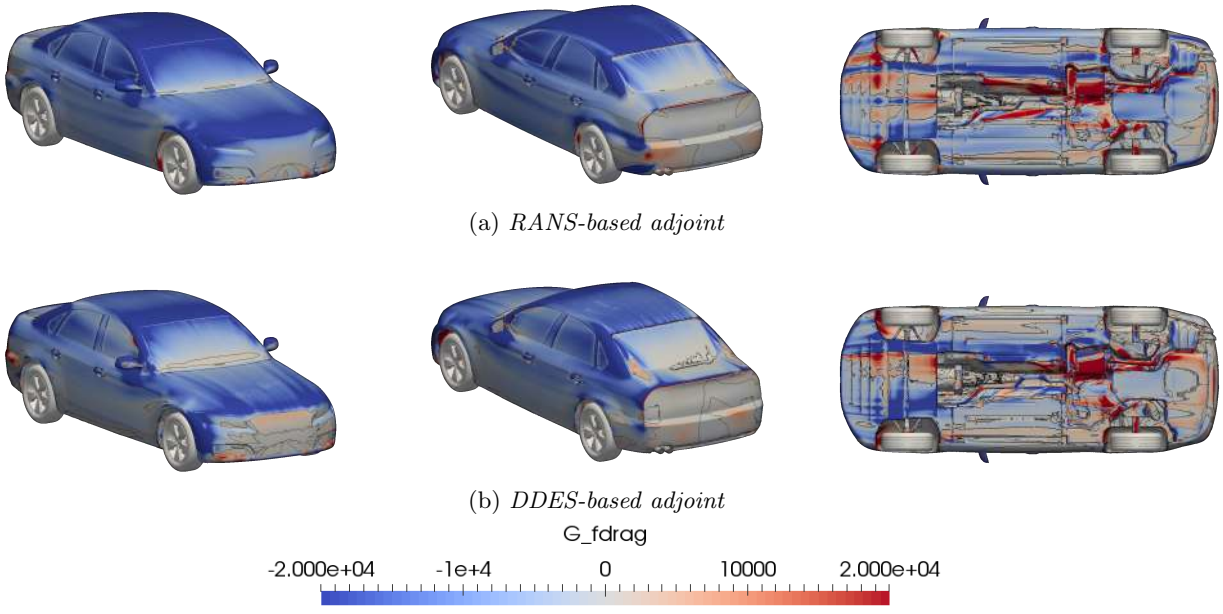

(a) *RANS-based adjoint*

(b) *DDES-based adjoint*

Figure 4.1: *Comparison of RANS-based and DDES-based sensitivity maps in notchback closed grill configuration*

4.2 Notchback open grill configuration

This section will investigate the notchback configuration with open grill. The primal flow fields and adjoint fields for the baseline geometry will first be presented. Several regions are selected and morphed to validate the trends of the sensitivity map.

4.2.1 Baseline

The simulation results consisting of the primal and the adjoint fields of the baseline model are presented here. As the primal input has a considerable influence on the adjoint solution, it is presented in the first place. The convergence assessment, pressure and velocity fields are discussed. The adjoint flow is considered to be converged once the sensitivity field stays constant independent of time step increment. The difference between the sensitivity fields based on the RANS primal and DDES primal is discussed in the end.

Primal field

Figure 4.2 shows the evolution history of C_dA for both the steady state and the transient simulations. It can be seen that the RANS primal cannot reach to a real steady state for such a complex vehicle geometry but the C_dA starts to oscillate over a certain small value (approximately 0.005 C_dA) after a number of iterations. Here 15000 iterations guarantee a quasi-converged state and the last 1000 iterations are averaged to eliminate the periodical oscillation. For the DDES primal, the 3s average time seems to be sufficient since the cumulative mean value goes close to the period mean value quite fast and they become identical before the end time.

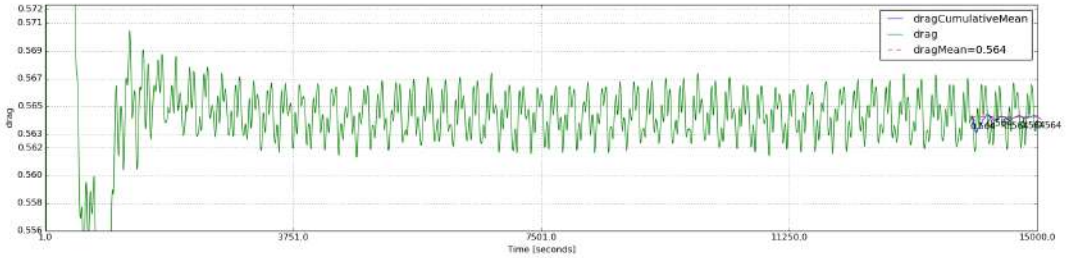

(a) *Drag factor C_dA of RANS primal*

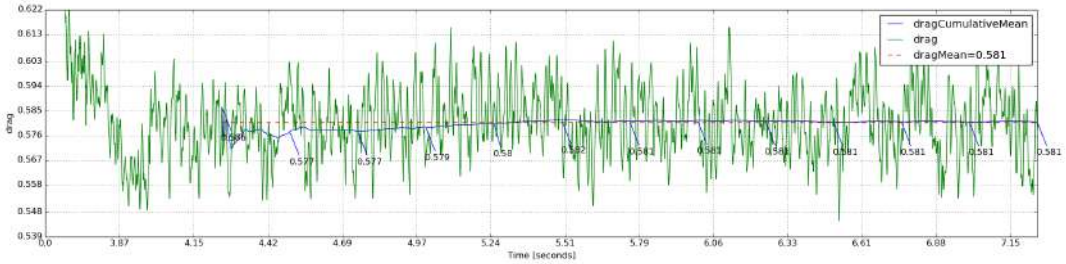

(b) *Drag factor C_dA of DDES primal*

Figure 4.2: *Evolution of drag factor C_dA for RANS and DDES primal in notchback configuration*

The velocity profiles along the y=0 plane for RANS and DDES simulations, in conjunction with streamlines coloured by pressure coefficient Cp, are shown in Figure 4.3. It is clear that the velocity is relatively low near the front grill then the air gets accelerated through the hood and reaches the highest when passing the roof. Behind the vehicle, a wake zone is formed with low velocity and flow separation. As to the pressure distribution, a relative high pressure zone is found in the front as shown by the red part of the streamlines whilst the rear end experiences a low pressure. It is this pressure difference that contributes the main proportion of the total drag.

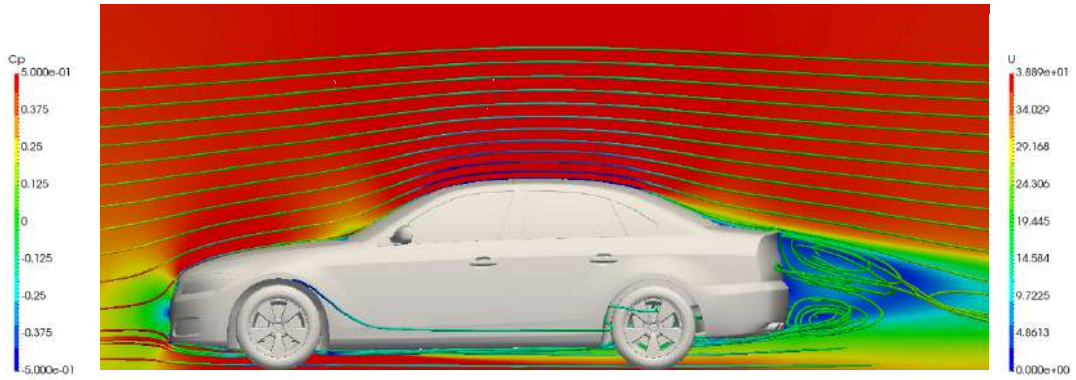

(a) *Plane y-0 for RANS primal*

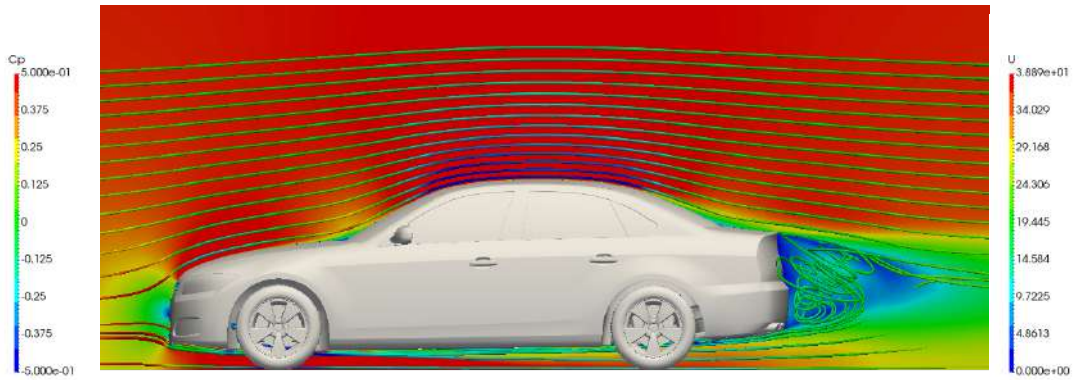

(b) *Plane y-0 for DDES primal*

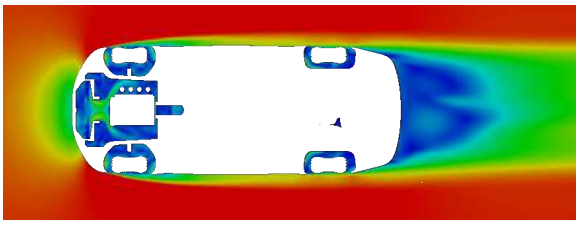

(c) *Plane z-0.2 for RANS primal*

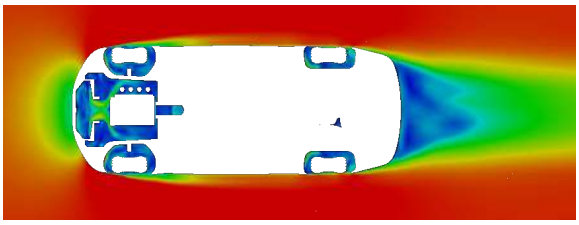

(d) *Plane z-0.2 for DDES primal*

Figure 4.3: *Pressure and velocity profiles of plane cuts for both RANS and DDES primal flow in notchback configuration*

It can also be seen that the RANS primal produces a larger wake zone than the DDES primal. A plane cut of z=0.2 shown in Figure 4.3c and 4.3d not only confirms the wake zone difference but also tells more regions including the vicinity of the front and rear wheels where small scale of detachment occurs. One more noticeable thing is that the wake zone is asymmetrical which is caused by the asymmetric underbody.

Adjoint field

To evaluate the convergence of the adjoint flow, several probes located around the vehicle are chosen to monitor the surface sensitivity field G-fdrag. The evaluation of the G-fdrag is shown as a function of iteration number in Figure 4.4. The picture of the exact probe locations is attached in Appendix. It can be seen that the RANS-based adjoint needs at least 8000 iterations to converge while the DDES-based adjoint requires approximately 10000 iterations. The evolution of the sensitivity field G-fdrag in RANS-based and DDES-based adjoint is found in Figure 4.5 and Figure 4.6 respectively. A large change (e.g. in the rear trunk) is observed during the first 5000 iterations in both states while a quasi-converged state is reached after around 10000 iterations. This is consistent with the results from the probes monitoring.

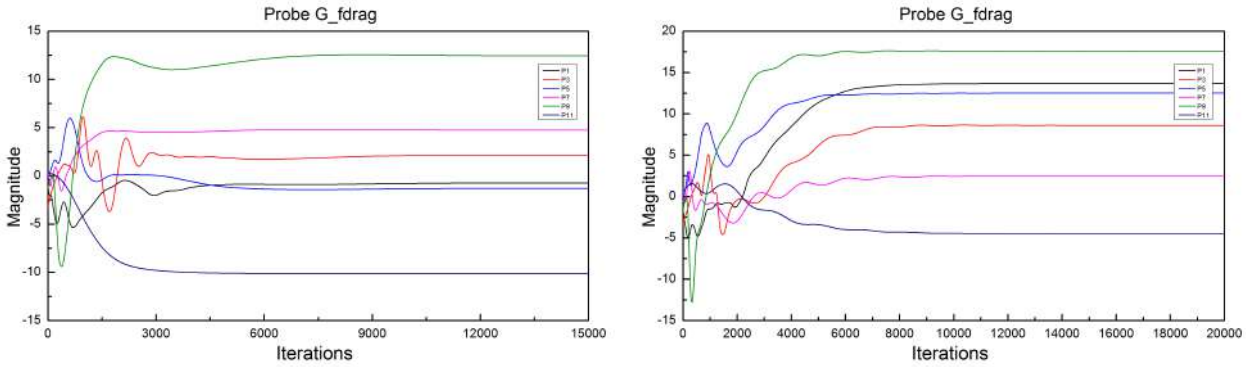

(a) *RANS-based adjoint* (b) *DDES-based adjoint*

Figure 4.4: *Probes monitor of sensitivity field G-fdrag in notchback configuration*

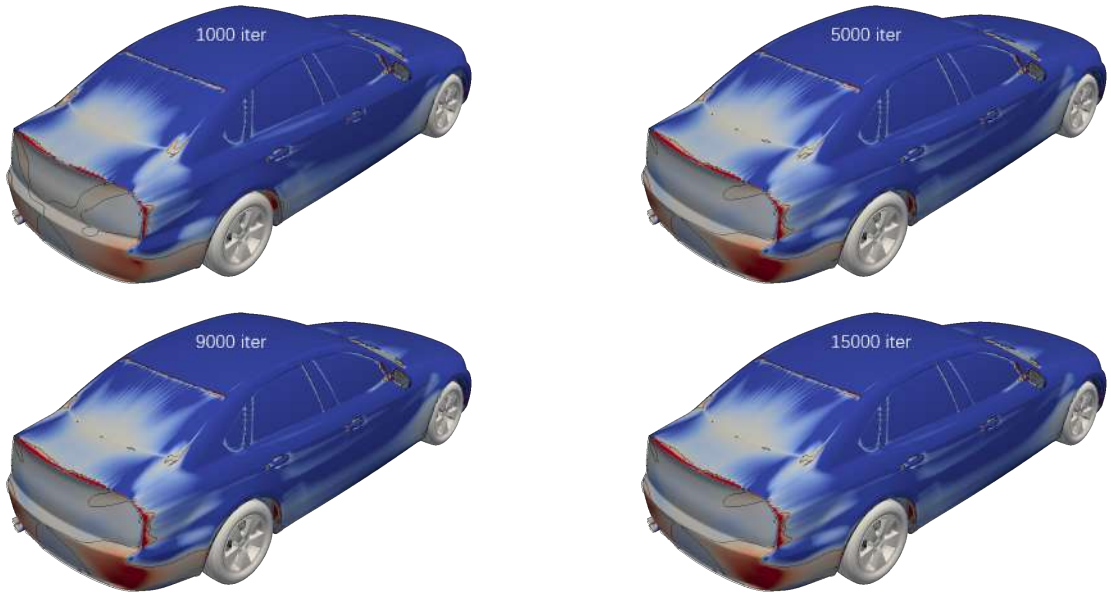

Figure 4.5: *Evolution of sensitivity map for RANS-based adjoint in notchback configuration*

The sensitivity field as computed by RANS-based and DDES-based adjoint is compared in Figure 4.7. On the largest part of the body (e.g. the roof and the hood), a similar trend shown by dark blue is observed. This is reasonable as a smaller exterior is expected to reduce drag. Significant differences occur in the regions where flow is detached. One region is the base of the front windshield on which the DDES-based adjoint predicts a larger outward region (the area inside the black contour line 0 on the windshield) than RANS-based adjoint. The difference is caused by the flow detachment in that region. Analogously, the rear windshield has the same trend. The opposite prediction is observed in the rear end of the vehicle, e.g. the edge around the rear trunk lid. The RANS-based adjoint suggests an upward rear spoiler while the DDES-based adjoint prefers a downturn. As the rear end region experiences large detachment and even separation, the DDES-based prediction seems to be more accurate than the RANS but it is difficult to conclude due to the lack of experimental data. Overall, the DDES-based adjoint produces more details than RANS-based adjoint on the largest part of the exterior. Another noticeable thing is that the asymmetry in the rear trunk exists in both states, the reason behind this is again the asymmetrical primal flow solution due to the underbody. As mentioned in Section 2.3, it is the primal field that determines the adjoint field solution in segregated approach for surface sensitivity calculation. Therefore, any characteristic in RANS and DDES primal fields (e.g. the separation prediction) will be reflected in the adjoint sensitivity maps.

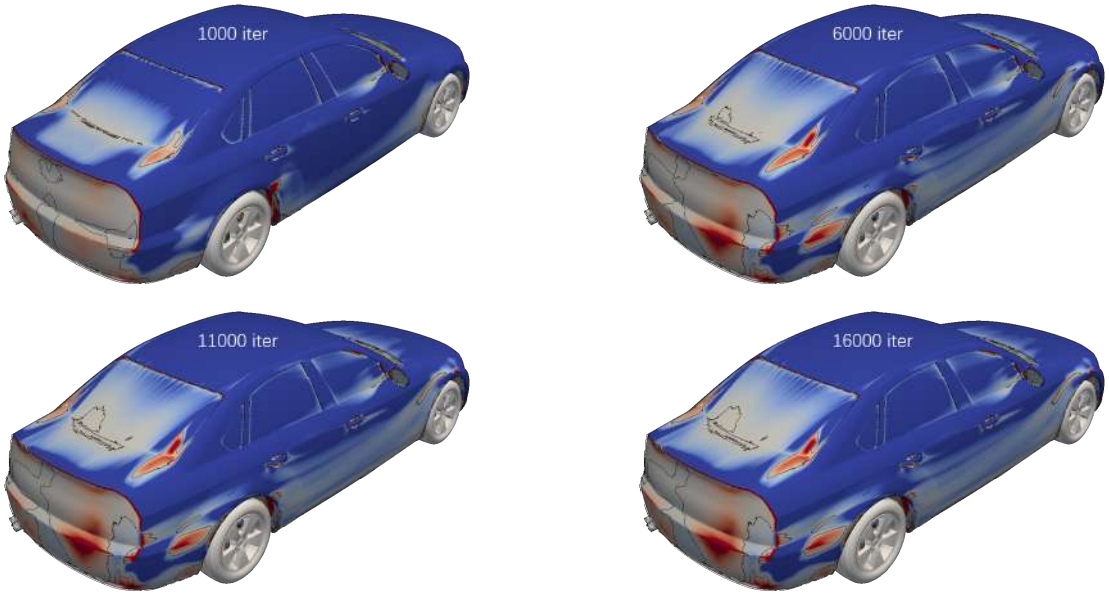

Figure 4.6: *Evolution of sensitivity map for DDES-based adjoint in notchback configuration*

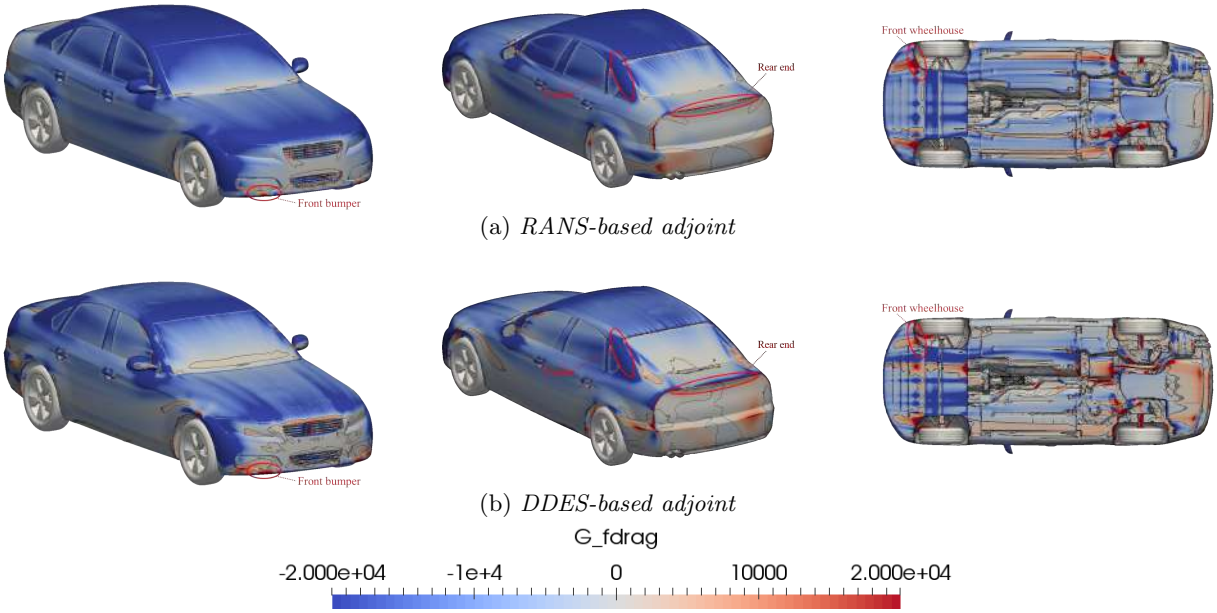

(a) *RANS-based adjoint*

(b) *DDES-based adjoint*

Figure 4.7: *Comparison of RANS-based and DDES-based sensitivity maps in notchback configuration*

To evaluate the trends predicted by the adjoint sensitivity field, four potential areas, highlighted in Figure 4.7, are morphed for both the steady state and the transient simulations. These regions are the front bumper, front wheelhouse, D-pillar and the rear end. For both states, the sensitivities suggest moving the selected area on the front bumper outwards. In the front wheelhouse area, a front wheel deflector is suggested and the D-pillar is expected to move inwards. Regarding the rear end, the results contradict each other and therefore the morphing will be done in two opposite directions based on the corresponding sensitivity map.

4.2.2 Front wheel deflector

The first area selected for morphing is in front of the front wheelhouse. This is the area where a front wheel deflector is often located and has shown to be beneficial for aerodynamic drag reduction in [21]. The morphing is done by node-based shape sensitivity morphing method for both the steady state RANS and the transient DDES cases. The deformed geometries are shown in Figure 4.8. FWD-RANS and FWD-DDES stand for the morphed geometries based on the steady state and transient surface sensitivities. The deflector in FWD-RANS has a maximum height of 20mm and a length of 180mm around the edge of front wheelhouse. For FWD-DDES, the deflector has a height of 15mm and a short length of 160mm but it is smoother than the one in FWD-RANS.

(a) *Baseline geometry* (b) *FWD-RANS* (c) *FWD-DDES*

Figure 4.8: *Geometry configurations of front wheel deflector*

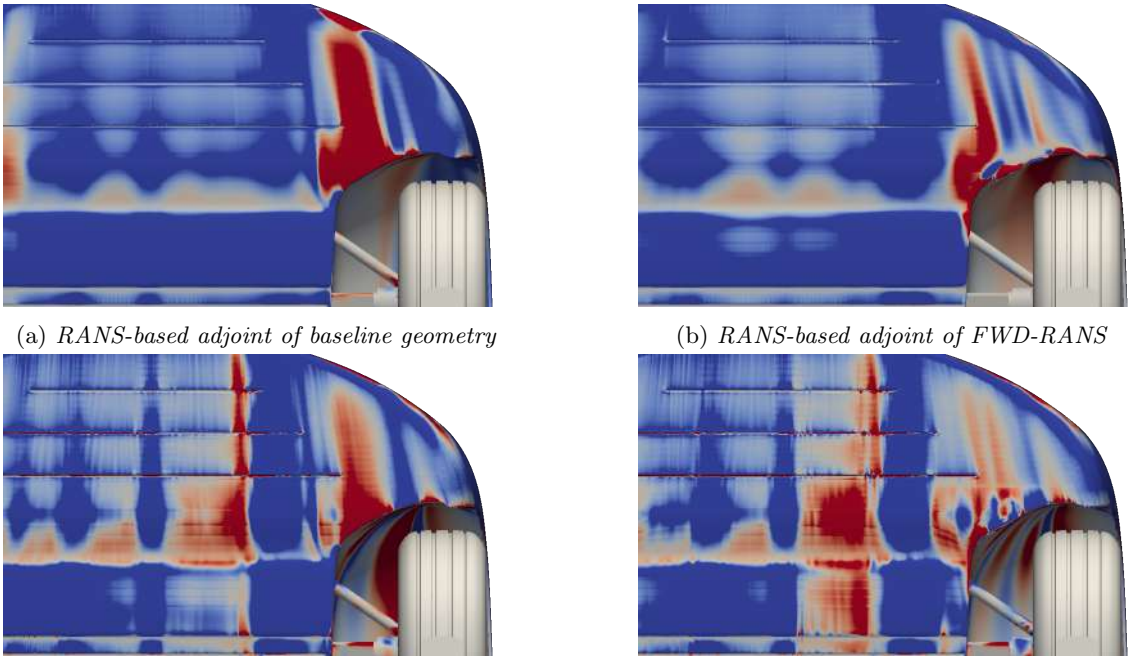

(a) *RANS-based adjoint of baseline geometry* (b) *RANS-based adjoint of FWD-RANS*

(c) *DDES-based adjoint of baseline geometry* (d) *DDES-based adjoint of FWD-DDES*

Figure 4.9: *Sensitivity map evolution before and after adding the front wheel deflector*

After re-simulations of the morphed geometries, FWD-RANS gets a 0.006 lower C_dA than the baseline-RANS case whilst for the FWD-DDES case, a 0.005 C_dA decrease compared to the baseline-DDES case is obtained. The comparison between the surface sensitivities in the front wheelhouse region before and after adding the deflector is presented in Figure 4.9. The red region in the baseline case has disappeared in the morphed geometries, both for RANS-based and DDES-based adjoint. Another noticeable thing is that a new red area at the side of the deflector appears and the reason behind is that the air flow is deflected sideways. For further improvement, the geometry morphing can be done based on the new sensitivity field.

A deformation of 20mm, as applied here, is quite large as the adjoint sensitivity map only represents the gradient of the drag with respect to a normal motion of the surface. It is on the other hand known that the front wheel deflectors can be significantly larger.

4.2.3 Front bumper

The front bumper morphing is performed using shape sensitivity morphing and the morphing regions for the steady state and the transient simulations are shown in Figure 4.10. The sensitivity map inside the red circle show the sensitivities controlling the deformation. It can be seen that although the sensitive region in the steady state and the transient simulations are slightly different, the tendency of both states is similar suggesting an outward moving front bumper. It is important to note that the geometry for steady state simulations in Figure 4.10b only differs with the original geometry in the investigation region while the morphed geometry for transient simulations in Figure 4.10c has a larger deformation region than the interested sensitivity zone. This is because the selection of deformation entities, as discussed in Section 3.5.1, in two states are different. A series of maximum displacements for the geometries in steady state and transient simulations are also accessed.

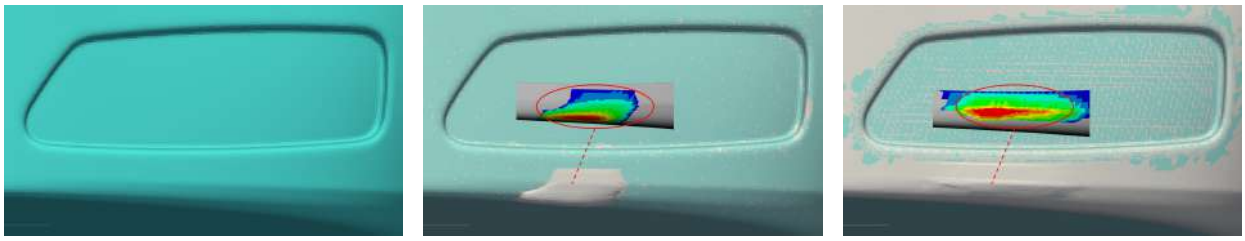

(a) *Front bumper original geometry* (b) *Geometry for steady state simulation* (c) *Geometry for transient simulation*

Figure 4.10: *Front bumper geometry before and after morphing in steady state and transient simulations*

Table 4.1: Validation result of front bumper

Case	Steady state		Case	Transient	
	Displacement	$\Delta\ C_dA$		Displacement	$\Delta\ C_dA$
A	2mm	-1	E	3mm	-1
B	5mm	-1	F	5mm	-1
C	6mm	0	G	8mm	+1
D	5+3mm	-3	H	15mm	+1

Note: 5+3mm means the geometry is first morphed 5mm based on the baseline sensitivity and then re-morphed 3mm further based on the sensitivities obtained in Case B.

Table 4.1 summarises the validation results for the morphed cases in the steady state and the transient simulations. The sensitivity maps before and after morphing in each state for each displacement are compared from Figure 4.11 to Figure 4.14.

For the steady state simulations, the drag factor C_dA is reduced except for Case C in which no improvement is obtained. Figure 4.12 shows that the sensitivity field gets smaller and less critical as the front bumper moves outward compared to the baseline case. This decaying phenomena of the sensitivity map may be not that visible for cases with small displacement (e.g. Case A), but it is obvious in Case D where the geometry is morphed twice. Therefore the largest part of the red region, in the RANS-based adjoint baseline as shown in Figure 4.11, has disappeared in Case D as seen in Figure 4.12d.

In the transient simulations, a drag improvement is obtained for cases with small displacement but failed for large displacement. As shown in Figure 4.10c, the morphing process not only moves outwards of the selected region but also the vicinity. However, the sensitivity map of the DDES-based adjoint baseline in Figure 4.14 shows that the vicinity of the focused red region is filled with neutral white and dark blue, which indicates an inward moving to reduce drag. Therefore, the outward moving vicinity in the morphed geometry is counter acting on drag reduction. Although the displacement of the vicinity is rather small compared to the investigation region, the area is large. This can lead to a negative contribution that is high enough to compensate and even overtake the positive improvement in cases with large displacement.

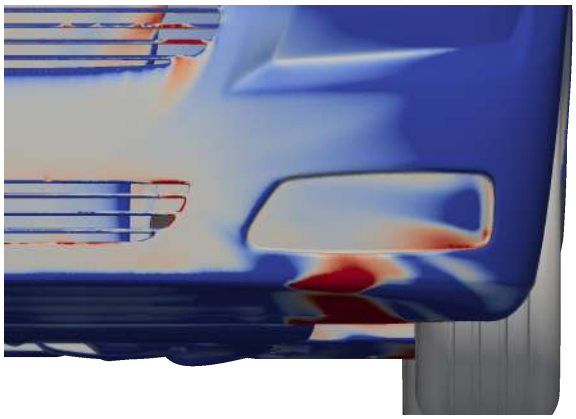

Figure 4.11: *RANS-based adjoint sensitivity map of front bumper baseline*

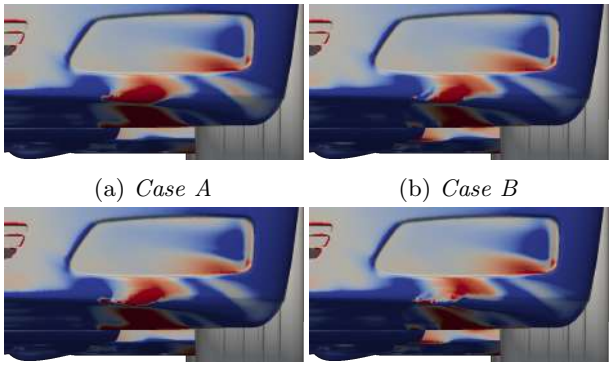

(a) *Case A* (b) *Case B*

(c) *Case C* (d) *Case D*

Figure 4.12: *Comparison of RANS-based adjoint sensitivity map for various displacement cases*

For example, the red region in Case H is showing a smaller red region but simultaneously the blue region in the vicinity (the bottom edge of the front bumper and side fender) is increased, which together yield a even higher drag. In Case E and F, the drag is improved due to that the small maximum displacement in the investigation region has almost negligible deformation effect on the vicinity. The sensitivity map in Figure 4.14a and 4.14b therefore has a clear red region decrease but no visible increase of the blue region.

Figure 4.13: *DDES-based adjoint sensitivity map of front bumper baseline*

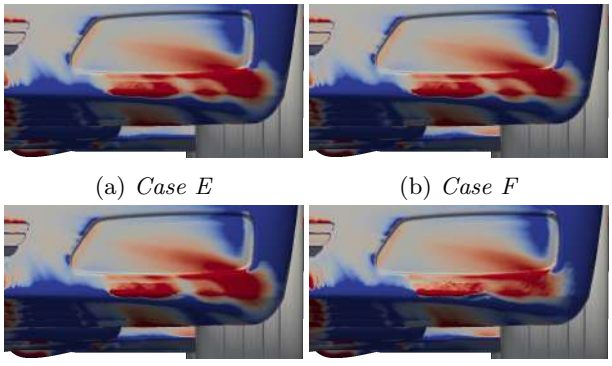

(a) *Case E* (b) *Case F*

(c) *Case G* (d) *Case H*

Figure 4.14: *Comparison of DDES-based adjoint sensitivity map for various displacement cases*

4.2.4 D-pillar

Figure 4.15 shows the pressure difference between the roof and the underbody where the flow speeds are different. Although the main consequence is the lift generation, the equally important consequence is that the air on the underbody tends to flow up to the sides, and towards the oblique rear top-surfaces. When the air meets the high speed flow from the roof, the vortices are invoked in the wake, as the 3-D streamlines shown in Figure 4.15a.

These vortices are called trailing vortices[22]. Energy loss in the swirling mass flow which represents another type of pressure drag, trailing vortex drag. The swirling flow with a high speed always occurs with a low pressure region[22]. Thereby, these vortices draw air away from the rear which also contributes to a low pressure behind the trunk. This low pressure pulls the flow further down to the floor causing more vortex and backward flow later, and at the same time the vortices will reinforce a lower pressure behind the rear. Consequently, this pressure drop in the rear increases the total pressure drag.

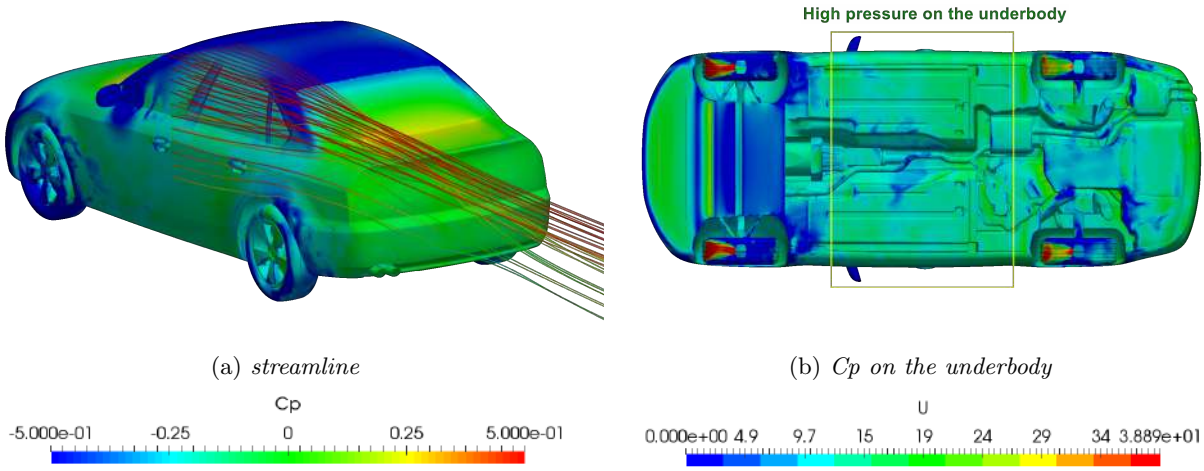

(a) *streamline* (b) *Cp on the underbody*

Figure 4.15: *Streamline and pressure distribution around D-pillar*

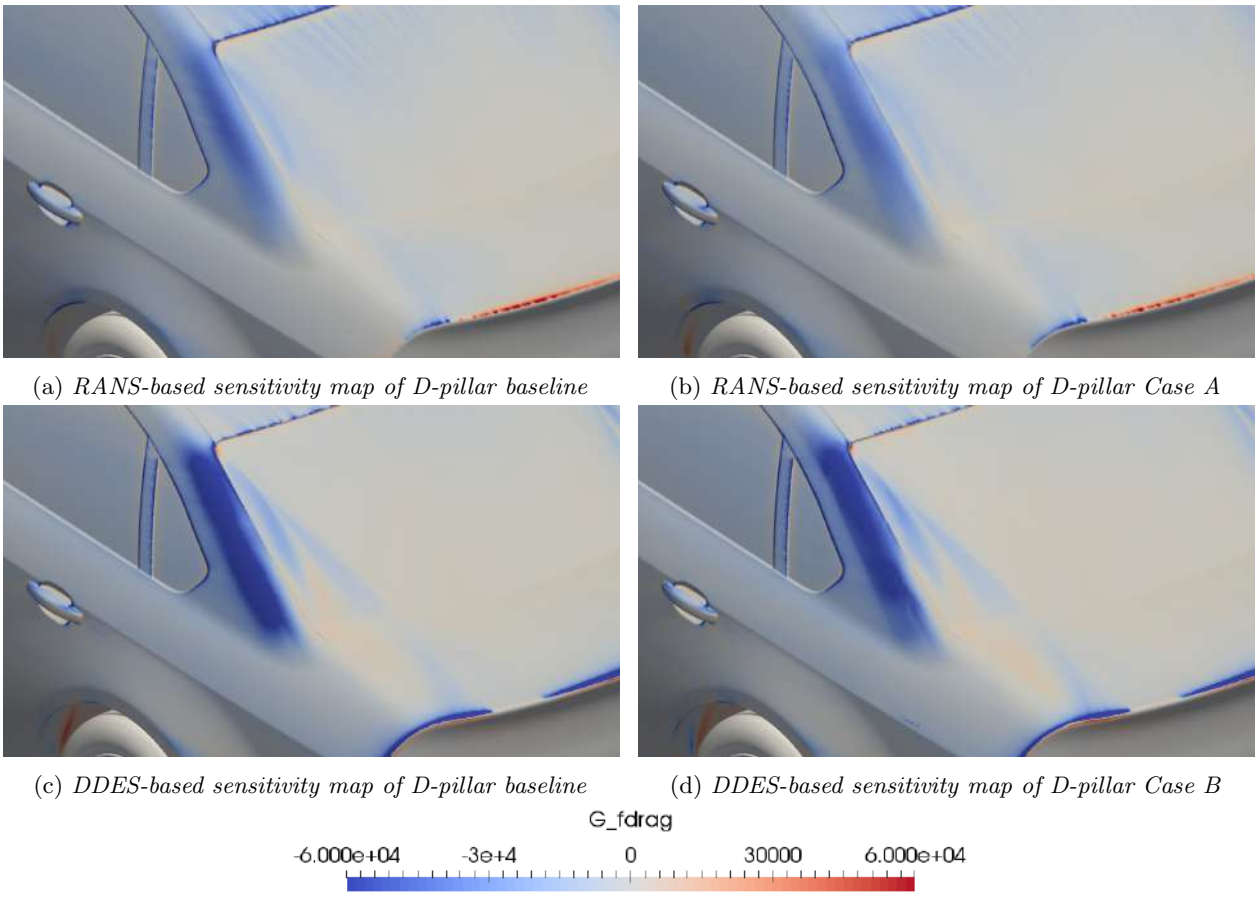

(a) *RANS-based sensitivity map of D-pillar baseline* (b) *RANS-based sensitivity map of D-pillar Case A*

(c) *DDES-based sensitivity map of D-pillar baseline* (d) *DDES-based sensitivity map of D-pillar Case B*

Figure 4.16: *Sensitivity map evolution before and after the D-pillar modification*

As seen in Figure 4.16a and 4.16c, both RANS-based and DDES-based adjoint predict similar trend at the D-pillar. In order to minimise the difference of morphing between steady state and transient, the same morphed entities and sensitivities area are selected as well as the same displacement, which yields similar morphed geometries.

The results for the morphed geometries are presented in Table 4.2. Both the steady state and the transient simulation yield 2 points of reduction in C_dA. This improvement is also illustrated by the sensitivity map evolution as shown in Figure 4.16. The sensitivities of the morphed geometry show that the blue region is getting smaller and less critical than the original case as the D-pillar moves inwards. The evolution may not be obvious since the morphing displacement is small, only 5.5mm maximum displacement.

Table 4.2: Results from the modification of the D-pillar based on shape sensitivity morphing

State	Case	Displacement	C_dA	ΔC_dA
Steady state	Baseline		0.564	
	A	-5.5mm	0.562	-0.002
Transient	Baseline		0.581	
	B	-5.5mm	0.579	-0.002

From the aerodynamics point of view, the inward moving D-pillar increases the slant angle which could weaken the trailing vortex and delay the separation. This improvement could be confirmed by the pressure distribution in the vicinity of D-pillar, as seen in the highlighted blue circles in Figure 4.17a. The low pressure region decreases, which means the adverse pressure gradient gets lower, this mitigation will decrease the risk of separation to some extent. The pressure distribution improvement in the rear trunk is shown in Figure 4.17c. The main difference is in the right-upper corner and left-upper corner (white circles). Compared with the baseline, Case B has a larger and higher pressure region in both corners. The sensitivities in Figure 4.16 show that a further potential to decrease the drag. Simultaneously, the weakness of the upper vortex results in a lower lift force as a bonus point, the lift coefficient decreased by 0.007 in case B.

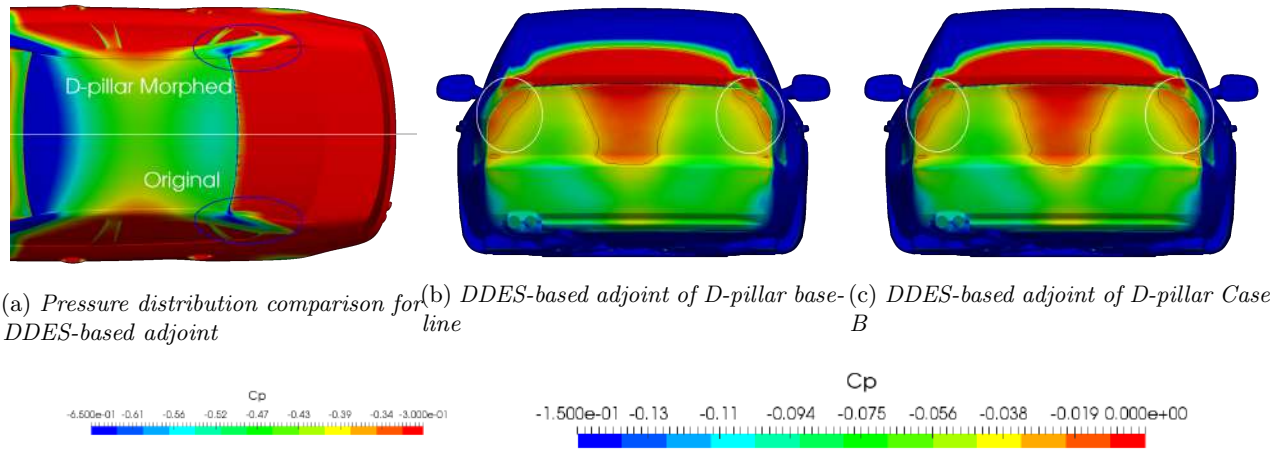

(a) *Pressure distribution comparison for DDES-based adjoint* (b) *DDES-based adjoint of D-pillar baseline* (c) *DDES-based adjoint of D-pillar Case B*

Figure 4.17: *Cp comparison in rear trunk for DDES-based adjoint*

4.2.5 Spoiler

Because of the high pressure in the vicinity of the base of the rear windshield, when the air flows over the windscreen, it tends to swirl with the flow from the sides, which generates conical vortices and begins to separate between the D-pillar and the rear. Besides, the separation is inevitable when the resultant flows encounter a sharp edge, for instance the end of the trunk. The separation phenomena is always followed by the bubbles of recirculation and vortices which are sources of drag[22]. Radiusing and tapering the rear end could produce significant drag reduction because the flow is kept to be attached as far back as possible. Generally, the rear pressure should be raised as much as possible so that the total pressure drag could be reduced. In this section, the improvement according to the sensitivities for the spoiler region will be presented. Additionally, not only is the shape sensitivity morphing performed, but also the direct morphing is introduced for the sake of an accurate validation.

Shape sensitivity morphing for spoiler

As mentioned in Section 4.2.1, the rear end of the trunk lid shows contrary results for when comparing the results from RANS-based adjoint to DDES-based adjoint. The sensitivity map is shown in Figure 4.18a and 4.18d. The RANS-based adjoint predicts an upturn for the rear edge (red region in Figure 4.18a) while the DDES-based adjoint indicates a downward and slightly backward modification (blue and small red stripe regions in Figure 4.18d).

To investigate this inconsistency, the steady state simulations will not only validate the morphed geometry based on the RANS-based adjoint sensitivities but also the one based on the DDES-based adjoint results and vice verse. The geometry configurations, geometry A and B, are shown in Figure 4.18. The region selected for morphing region selection in geometry A is a bit larger than the one in geometry B according to the sensitivity map.

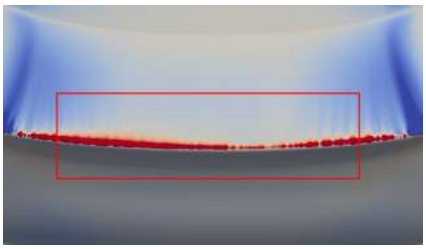

(a) *RANS-based adjoint*

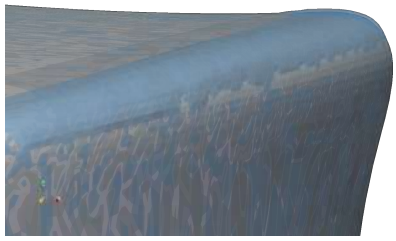

(b) *Original vs. geometry A (blue)*

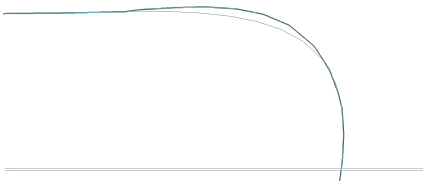

(c) *Outline, original vs. geometry A (green)*

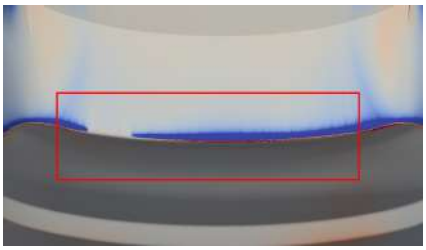

(d) *DDES-based adjoint*

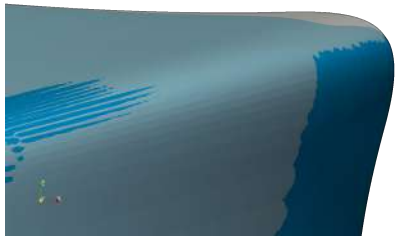

(e) *Original vs. geometry B (blue)*

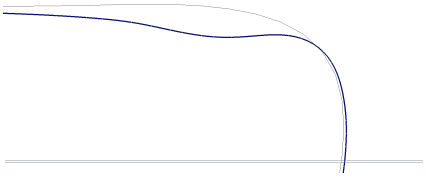

(f) *Outline, original vs. geometry B (blue)*

Figure 4.18: *Geometry configurations based on shape sensitivity morphing for RANS-based adjoint (upper) and DDES-based adjoint (lower) simulations*

Table 4.3: Results of different sensitivity morphings

State	Geometry Description	Case	Max. Displ.	C_dA	ΔC_dA	Note
Steady state	Baseline	—	—	0.564	—	—
	Geometry A^*	A	3mm	0.561	−0.003	Expected
	Geometry B	B	3mm	0.567	+0.003	Expected
Transient	Baseline	—	—	0.581	—	—
	Geometry B^{**}	C	3mm	0.583	+0.002	Unexpected
	Geometry A	D	3mm	0.585	+0.003	Expected

Note: *: Morphing based on RANS-based adjoint result.
**: Morphing based on DDES-based adjoint result.

Assume that the sensitivity map in both states is predicted correctly, then theoretically Case A and C in which the geometry is morphed according to its corresponding sensitivity map should produce a lower drag factor, while the control cases, Case B and D, should give higher drag since the morphed geometry moves in the direction of increased drag. The results for the baseline and the morphed geometries are presented in Table 4.3. All cases show good agreements with the expected trend of the drag force except for Case C which fails to produce a drag reduction. As explained in the previous section 4.1, only the qualitative accuracy is expected

from the sensitivities. Therefore, using the same maximum displacement to morph the geometries will not have the same impact on the drag reduction, which means 3mm may be appropriate for the cases based on RANS-based adjoint but inappropriate for the cases based on DDES-based adjoint.

Case A in Figure 4.19b shows that after deforming the rear based on the sensitivities, the the red critical region shrinks significantly compared with the RANS-based adjoint baseline in Figure 4.19a. While in Case B this reduction becomes even more noticeable, seen in Figure 4.19c, which conflicts with the prediction of the original sensitivity map, seen in Figure 4.19a. Because the steady state map shows the spoiler region should be bumped out rather than caved in, thus basically the cave-in geometry should have much more red sensitivity region in the spoiler, whereas the result goes to an adverse direction. This unanticipated sensitivities distribution is attributed to the cave-in spoiler shape in geometry B, seen in Figure 4.20a.

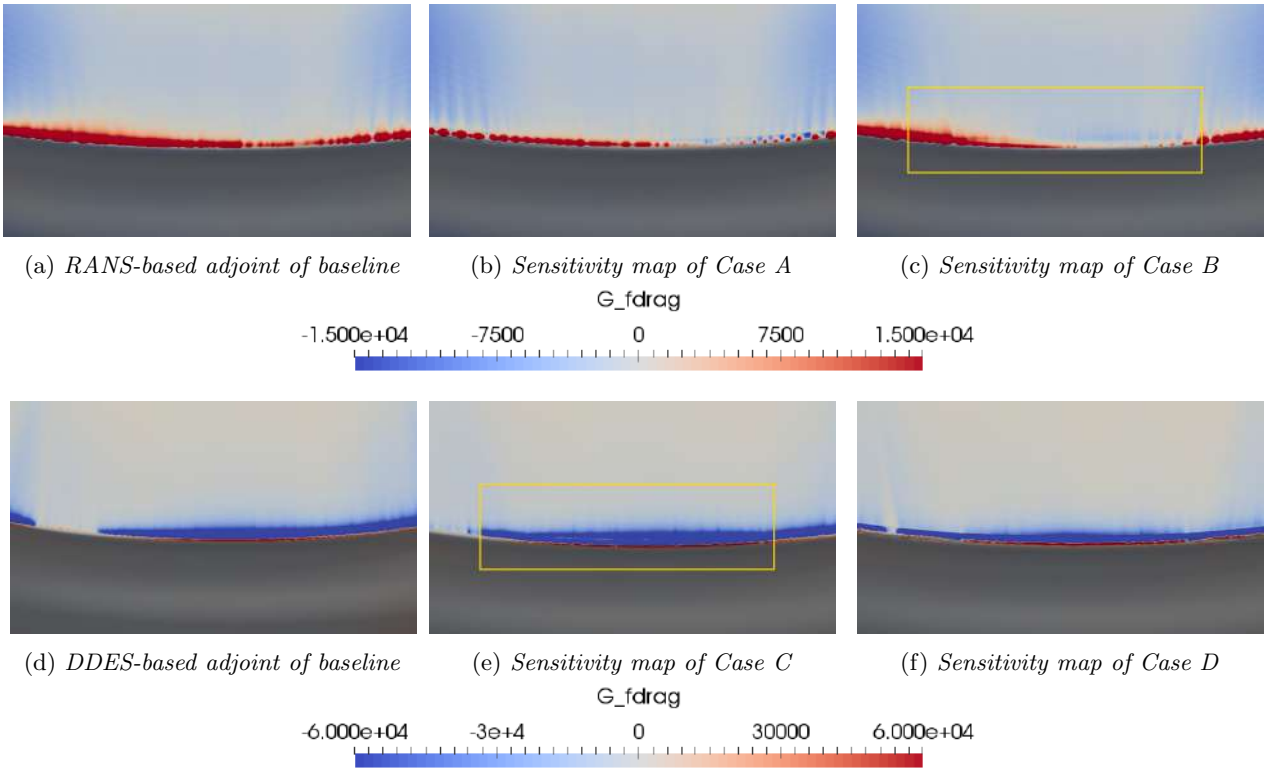

(a) *RANS-based adjoint of baseline* (b) *Sensitivity map of Case A* (c) *Sensitivity map of Case B*

(d) *DDES-based adjoint of baseline* (e) *Sensitivity map of Case C* (f) *Sensitivity map of Case D*

Figure 4.19: *Sensitivity map evolution before and after spoiler modification based on shape sensitivity morphing in RANS-based adjoint and DDES-based adjoint simulations*

Unfortunately, the sensitivity morphing can not get rid of the unsmooth issue, seen in Figure 4.20a, the rugged lid edge in the blue circle. It is very hard to draw a conclusion whether the adjoint solver predicts right or not, based on the results presented above. By using the sensitivity morphing, it is hard to guarantee a smooth geometry. Unsmooth geometry can easily result in an increase in drag. Therefore, an alternative morphing method is introduced in the next section.

Direct morphing

The sensitivity morphing in ANSA can easily result in an unsmooth geometry. Indeed, it is very easy to make the geometry worse if the selection is not appropriate and very unsmooth surfaces may be generated, see for example in Figure 4.20.

(a) *Geometry B by shape sensitivity morphing*

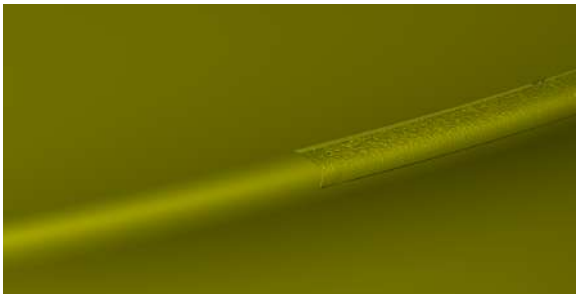

(b) *Original surface (left) vs. unsmooth sensitivity morphing*

Figure 4.20: *Un-smooth issue in shape sensitivity morphing*

One alternative morphing method is based on direct morphing, which makes it easier to obtain a smooth geometry. Figure 4.21 illustrates how the rear end is split into three parts. The upper piece is located in the blue region which will be deformed in negative z-dir, and for the lower piece, which is deformed in x-direction. The sensitivities imply that the morphing should be performed in the normal direction to the surface. Here the lower piece was only moved in x direction. It is hard to interpret if the sensitivities are implying an elongation of the trunk or a sharper edge on the rear. Another thing that should be mentioned here is that the absolute value of the blue part and the red part, the mean value in the blue region is almost 10 times over the one in the red region, which means the blue part is more sensitive for the drag reduction than the red region and is expected to give a larger decrease in drag. The direct morphing is only combined with the DDES-based adjoint sensitivities.

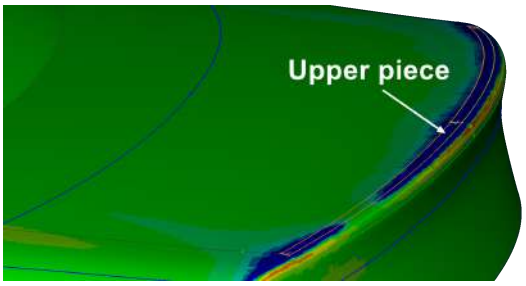

(a) *Upper piece with sensitivities for DDES-based adjoint*

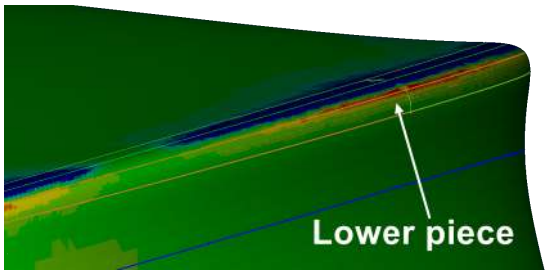

(b) *Lower piece with sensitivity map for DDES-based adjoint*

Figure 4.21: *Control entities with sensitivities for DDES-based adjoint*

Table 4.4: Results of different direct morphing

Group	Case	Morphing Direction	Displacement	C_dA	ΔC_dA
Baseline				0.581	
1	A	x-axial	3mm	0.582	+0.001
	B	x-axial	6mm	0.585	+0.004
2	C	x-axial	3mm	0.579	–0.002
		z-axial	-6mm		
	D	x-axial	6mm	0.577	–0.004
		z-axial	-6mm		
3	E	z-axial	-6mm	0.578	–0.003
	F	z-axial	-9mm	0.575	–0.006

Six cases are set up with different direction and displacement, they are divided into three groups, Group 1 for

x-axial deformation extending the rear on longitudinally, Group 3 for z-axial deformation shaping the vehicle rear to be more tapering, and Group 2 combines these two effects. All these six cases are morphed with the same displacement interval (3mm) either in *x-dir* and *z-dir* to adjust the deformation. The geometry after morphing can be seen in Figure 4.22 and the resulting drag change is presented in Table 4.4.

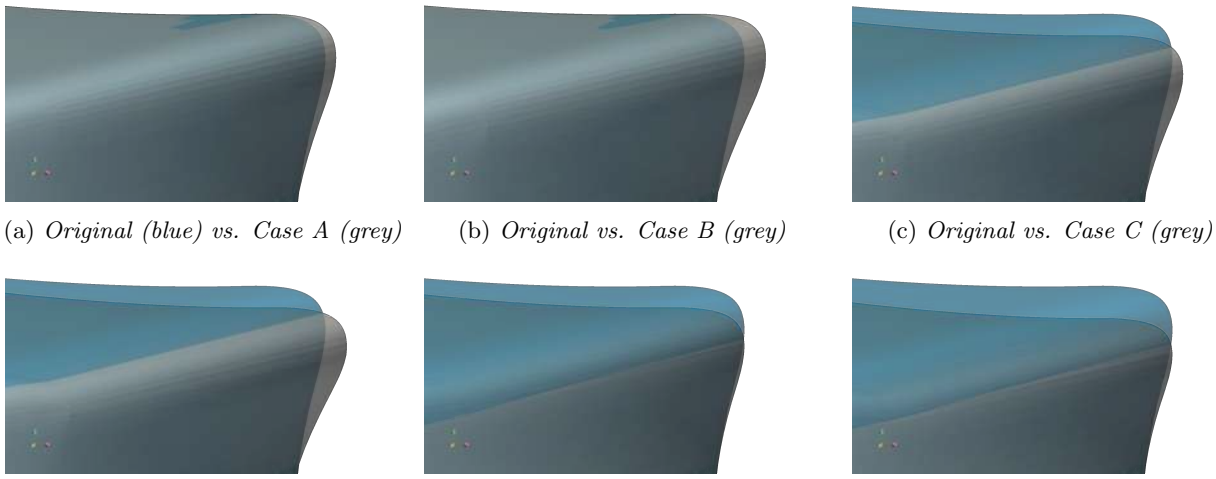

(a) *Original (blue) vs. Case A (grey)* (b) *Original vs. Case B (grey)* (c) *Original vs. Case C (grey)*

(d) *Original vs. Case D (grey)* (e) *Original vs. Case E (grey)* (f) *Original vs. Case F (grey)*

Figure 4.22: *Geometry configurations based on direct morphing for DDES-based adjoint simulations*

The results in Group 2, 3 show the drag reduction while the modifications done in Group 1, where the deformation is only performed in *x-dir*, results in a drag increase. One explanation for the drag increase in Group 1 is that the red region may want to make the edge much sharper rather than extending the trunk in the longitudinal direction. Also, the partition of the lower piece does not include the whole red region. These two factors in the direct morphing selection may contribute to this increase in drag.

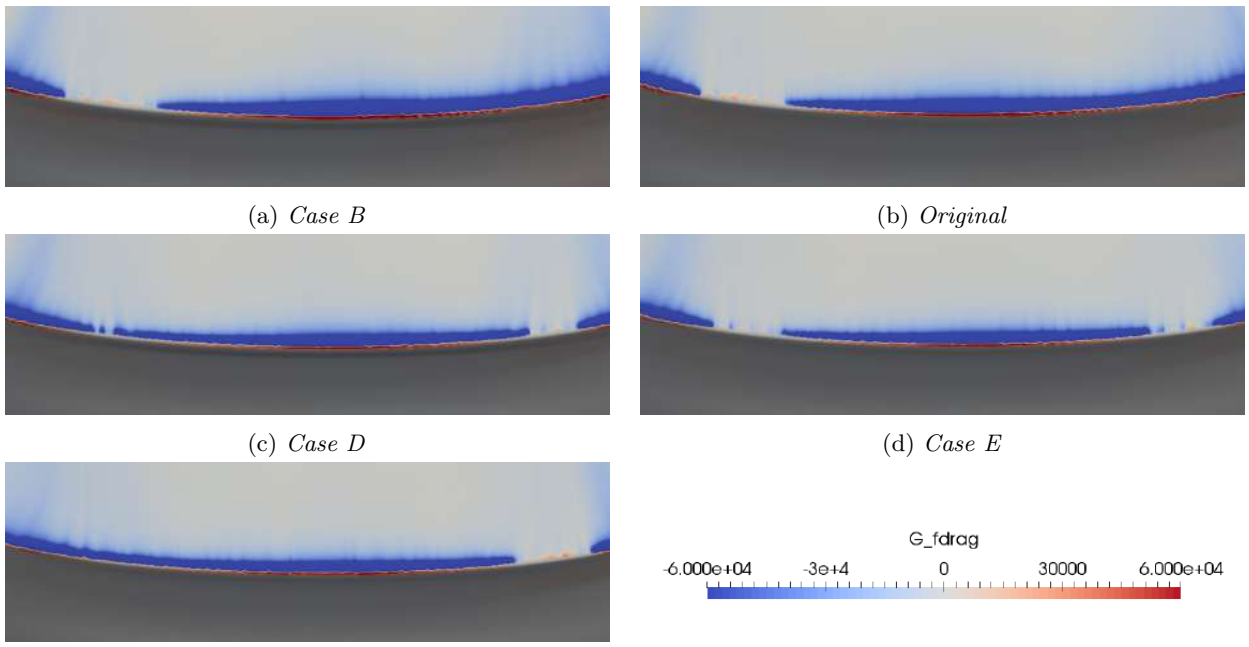

(a) *Case B* (b) *Original*

(c) *Case D* (d) *Case E*

(e) *Case F*

Figure 4.23: *Sensitivity map evolution before and after spoiler modification based on direct morphing in DDES-based adjoint simulations*

The rest four cases which obtain an obvious reduction well confirmed that blue region is very sensitive to the drag reduction. It also shows that tapering the rear is an effective way to reduce drag, which also is a well-confirmed benefit for drag reduction in aerodynamics.

The evolution of the sensitivity map is shown in Figure 4.23. The sensitivities on the rear for Case B, the case that that resulted in the highest drag, is shown in Figure 4.23a. It shows the largest critical area in Case B, while a smaller critical area for the other cases as a lower drag factor gained. But the blue region is still quite significant which indicate that the rear edge could be moved further downwards in order to decrease the drag further.

In conclusion, the downwards deformation of the spoiler for the notchback has a positive impact on the drag reduction which matches the prediction by DDES-based adjoint. The deformation is only valid in a limited range and useful for fine-tuning, a large deformation may easily go beyond the trend predicted by the adjoint-based sensitivity map.

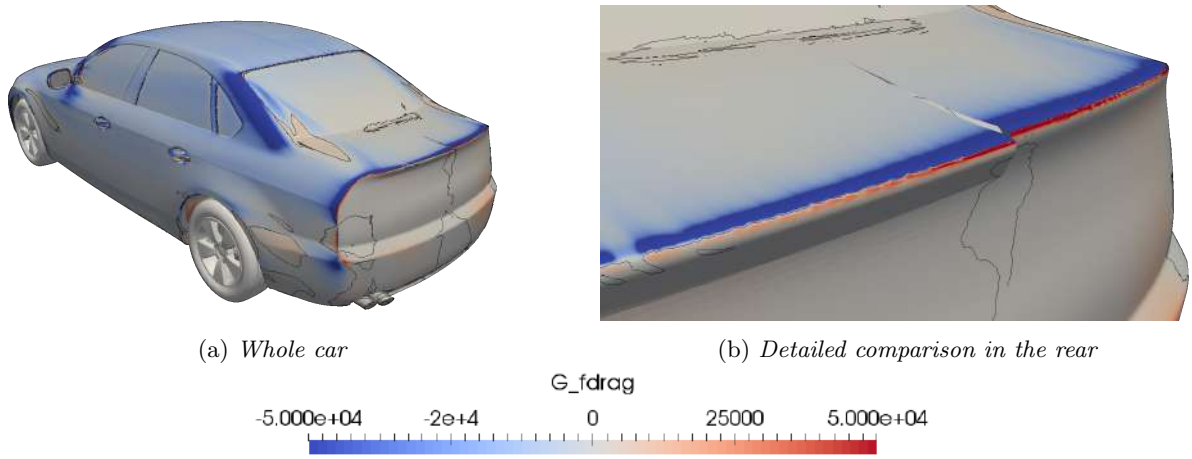

(a) *Whole car* (b) *Detailed comparison in the rear*

Figure 4.24: *Geometry comparison between Case D (left-half part) and original geometry (right-half part)*

4.3 Fastback configuration

The fastback configuration is very similar to the notchback but with continuously smoothed slope from the roof to the back.

4.3.1 Primal field

The evolution history of C_dA for RANS and DDES primal is shown in Figure 4.25. The RANS primal produces a quasi-steady result with a fluctuation of only 0.002 C_dA after a couple of thousand of iterations. The drag is quite close in both the RANS primal and the DDES primal simulations, 0.578 and 0.573 respectively.

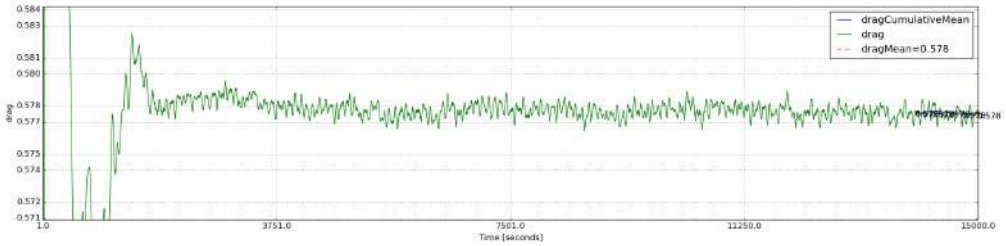

(a) *Drag factor C_dA of RANS primal*

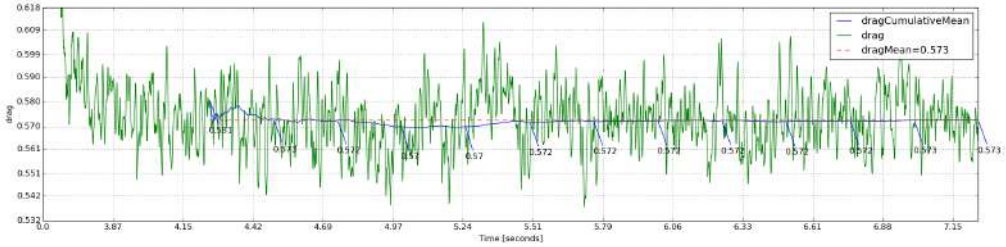

(b) *Drag factor C_dA of DDES primal*

Figure 4.25: *Evolution of drag factor C_dA for RANS and DDES primal in fastback configuration*

Figure 4.26 shows the velocity profile along y=0 plane in fastback configurations. It is evident that the flow is more attached to the vehicle surface and the flow field in both the RANS primal and DDES primal does not differ as much as that in notchback. This is not surprising since the fastback configuration has a smaller slant angle than notchback. The high velocity flow after the roof is then smoothly decelerated along the fastback and the detachment is delayed and minimised.

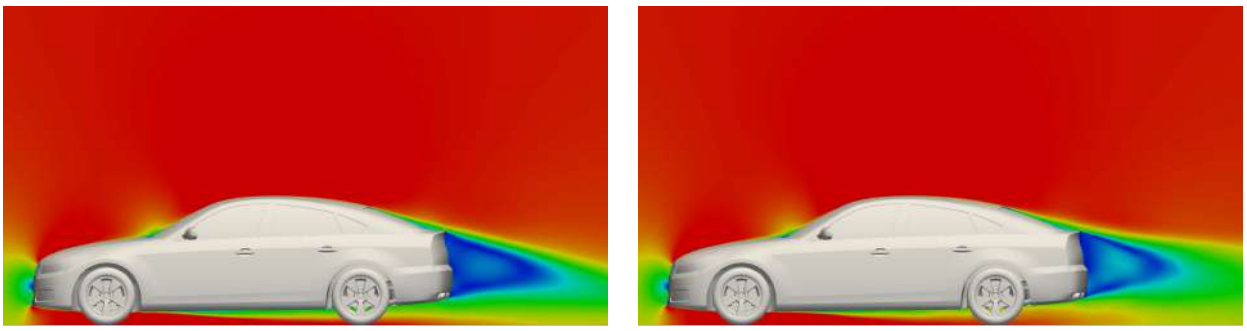

(a) *Plane y-0 for RANS primal*

(b) *Plane y-0 for DDES primal*

Figure 4.26: *Pressure and velocity profiles of plane cuts for both RANS and DDES primal flow in fastback configuration*

4.3.2 Adjoint field

Similar to the convergence assessment of adjoint flow in notchback, the sensitivity field in fastback is monitored by several probes around the car. The evolution of the sensitivity map is also checked for both RANS-based and DDES-based adjoint and the figure is attached in Appendix.

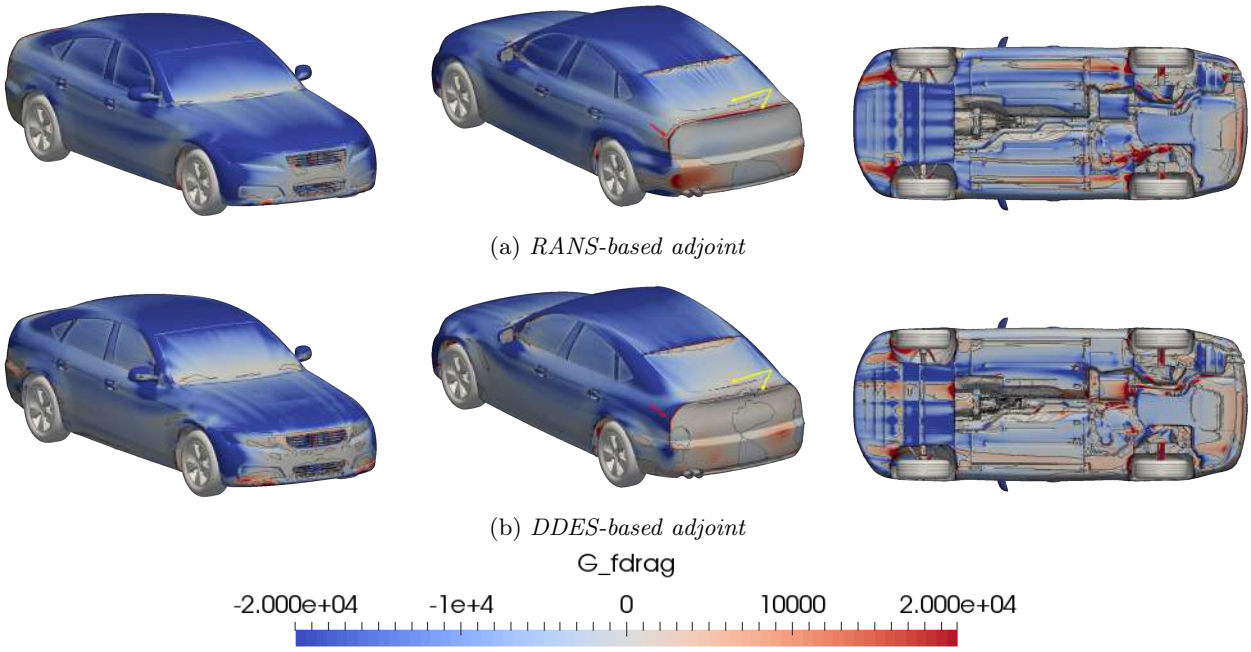

(a) *RANS-based adjoint*

(b) *DDES-based adjoint*

Figure 4.27: *Comparison of RANS-based and DDES-based sensitivity maps in fastback configuration*

Figure 4.27 shows the fully converged sensitivity maps computed for the fastback configuration. Looking from the front, the largest part of the exterior is coloured by dark blue in RANS-based and DDES-based adjoint and the sensitivity field distribution is very similar to the notchback configuration (seen in Figure 4.7). It is the rear regions of the vehicle where the primal flow feature differs that preserves evident sensitivity map difference between fastback and notchback. As discussed in the fastback primal flow section, the RANS primal and DDES primal produce similar flow fields due to the flow attachment in the rear. Therefore, the sensitivity map should not considerably differ in RANS-based adjoint and DDES-based adjoint. One noticeable region is the rear windshield on which a decent consistency is obtained from two states adjoint in fastback. On the rear truck edge, the sensitivity maps in fastback also demonstrate a similar pattern even though the RANS-based adjoint predicts a consecutive red stripe whilst the DDES-based adjoint's prediction is non-consecutive, shown in Figure 4.27a and 4.27b by the yellow arrows.

Besides the difference of sensitivity map in the rear trunk end, it is interesting to notice the contrary prediction from RANS-based adjoint and DDES-based adjoint on the rear side as highlighted by the red arrow. From the aerodynamic experience point, the dark blue prediction on the rear side from DDES-based adjoint is more meaningful than the opposite trend from RANS-based adjoint. This is because that tapering the rear side which makes the vehicle more "boat-tailing" has been proved to be productive for drag reduction [8].

4.4 Squareback configuration

The squareback configuration differs a lot from the notchback since its roof has been extended rearward over a passenger or cargo volume. The high slant angle could introduce a large wake zone which results in difference between the RANS and the DDES primal solutions.

4.4.1 Primal field

Figure 4.28 shows the evolution of C_dA for steady state and transient primal simulations for the squareback configuration. It can be seen that the C_dA in RANS primal fluctuates up to 0.010. This fluctuation is much stronger than that in notchback and fastback. The average over the last 1000 iterations is then not sufficient to

eliminate the periodical oscillation, and a longer average is used. For the DDES primal, the averaging time is increased from 3s to 4s.

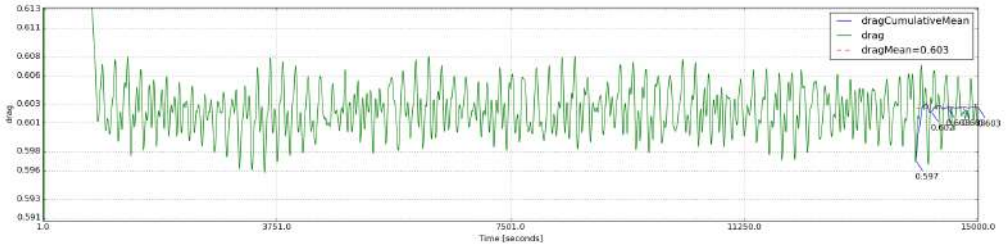

(a) *Drag factor C_dA of RANS primal*

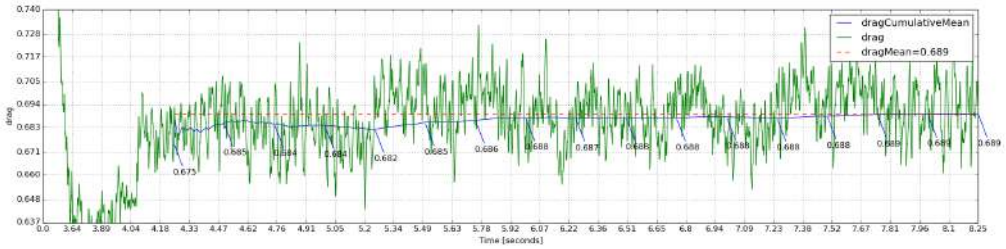

(b) *Drag factor C_dA of DDES primal*

Figure 4.28: *Evolution of drag factor C_dA for RANS and DDES primal in squareback configuration*

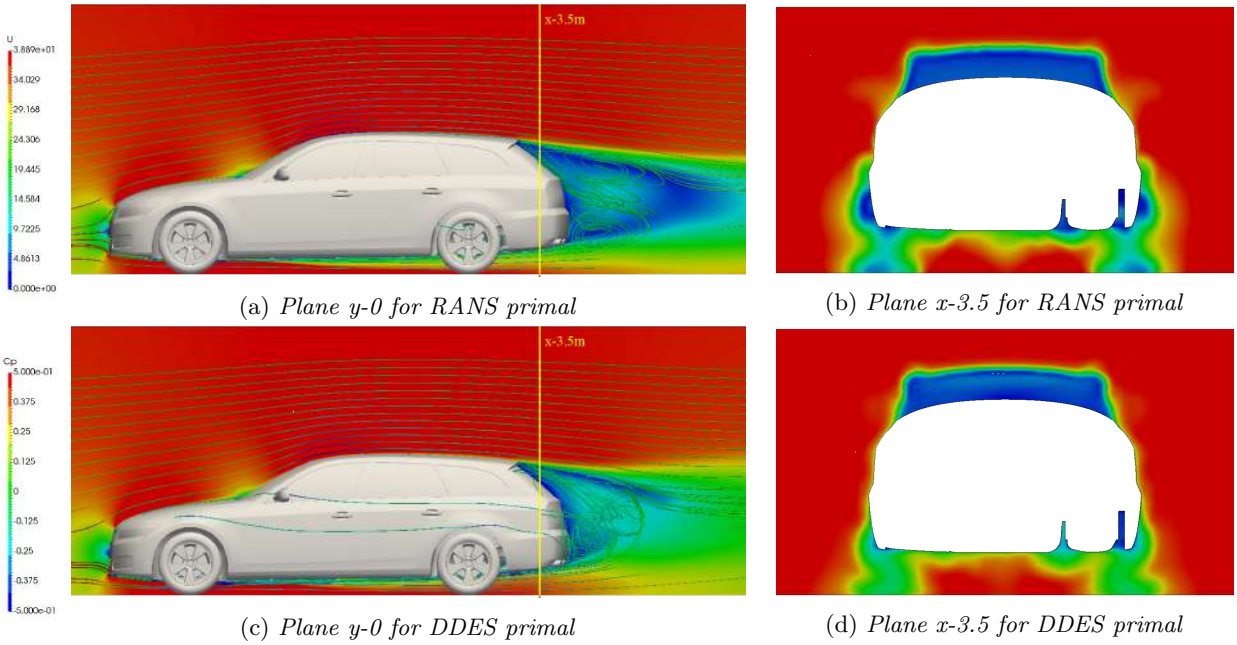

(a) *Plane y-0 for RANS primal*

(b) *Plane x-3.5 for RANS primal*

(c) *Plane y-0 for DDES primal*

(d) *Plane x-3.5 for DDES primal*

Figure 4.29: *Pressure and velocity profiles of plane cuts for both RANS and DDES primal flow in squareback configuration*

The velocity profiles with streamlines for the RANS primal and the DDES primal are illustrated in Figure 4.29. It is apparent that the RANS primal produces a large wake zone behind the vehicle with recirculations along the rear windshield and bumper. By contrast, the wake zone is smaller in DDES primal and the recirculations mainly occur in the bottom part of the wake. A x-normal plane cut in the rear of the squreback (x=3.5) is also taken to show the velocity field. One difference is observed at the side of the lower body where the RANS primal has a larger low velocity region than the DDES primal. The reason is that the flow in this region

is affected by both the rear wheelhouse disturbance and the recirculations from the bottom wake, which in combination contributes to the flow separation. This primal flow difference could be the possible explanation for the difference in the adjoint sensitivities in the corresponding region.

4.4.2 Adjoint field

The convergence of the adjoint fields in squareback is assessed in the same way as the other two back configurations and the evolution figure of sensitivity map is attached in the Appendix. The sensitivity maps in both RANS-based adjoint and DDES-based adjoint converged after roughly 10000 iteration and they are presented in Figure 4.30.

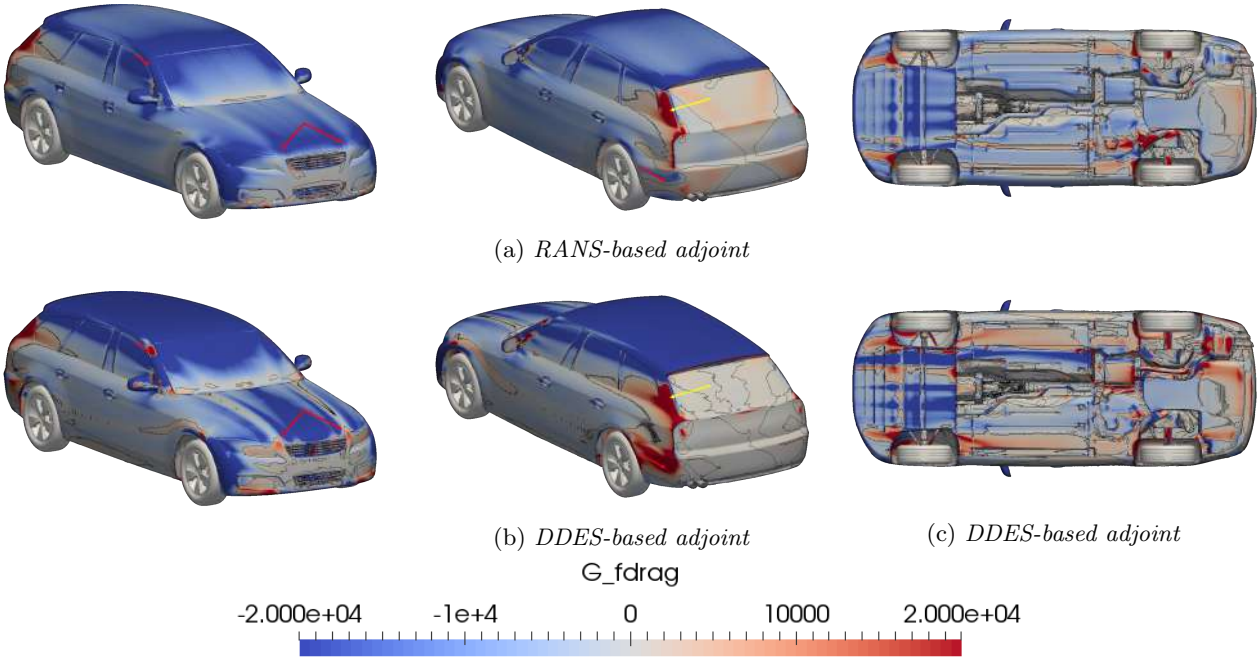

(a) *RANS-based adjoint*

(b) *DDES-based adjoint*

(c) *DDES-based adjoint*

Figure 4.30: *Comparison of RANS-based and DDES-based sensitivity maps in squareback configuration*

The sensitivity maps show similar trends in the largest part of the vehicle. Significant difference is though seen on the rear trunk end, this region is considerably influenced by the base wake. Several additional difference between RANS-based adjoint and DDES-based adjoint is preserved in the front, for example the sides of the front upper grill and the tip of the A-pillar as shown by the red arrows in Figure 4.30a and 4.30c. It is difficult to clarify the reason for the small red sensitivity areas predicted in DDES-based adjoint. One possibility is that even though the massive separation occurs in the rear end, it indeed affects the flow in the front to some extent.

In the rear side of the squareback, the RANS-based and DDES-based adjoint predict similar red outward region in the upper body (yellow arrow), but almost contrary trend in the lower body (red arrow) as seen in Figure 4.30a and 4.30b. As mentioned in the squareback primal flow field section (Figure 4.29b and 4.29d), the primal flow solutions for two states are not consistent. It is this difference in primal solution that leads to the difference in adjoint sensitivity maps.

5 Analysis of the Volvo XC90

This chapter presents the results from where the the DDES-based adjoint sensitivities are calculated on the Volvo XC90. The resulting sensitivity maps for both closed and open shutter configurations are presented.

5.1 Analysis of the sensitivity map

The XC90 model used in this thesis is very detailed, including components such as the engine bay, powertrain, cables, tubes etc., which makes the mesh size is twice as high as the DrivAer model. The averaging time period of the primal flow should also be sufficiently long to ensure that the primal field is fully converged before the flow fields is passed into the adjoint solver. The same setup of the primal field is applied for XC90 model as was done in the DrivAer model, but the averaging period is increased to 6s, and same for the adjoint field. Additionally, the wheel rotation was also simulated using MRF for the wheels in order to see the impact on the sensitivity map. The sensitivity maps for closed, open shutter without MRF and open shutter with MRF conditions are presented in Figure 5.1.

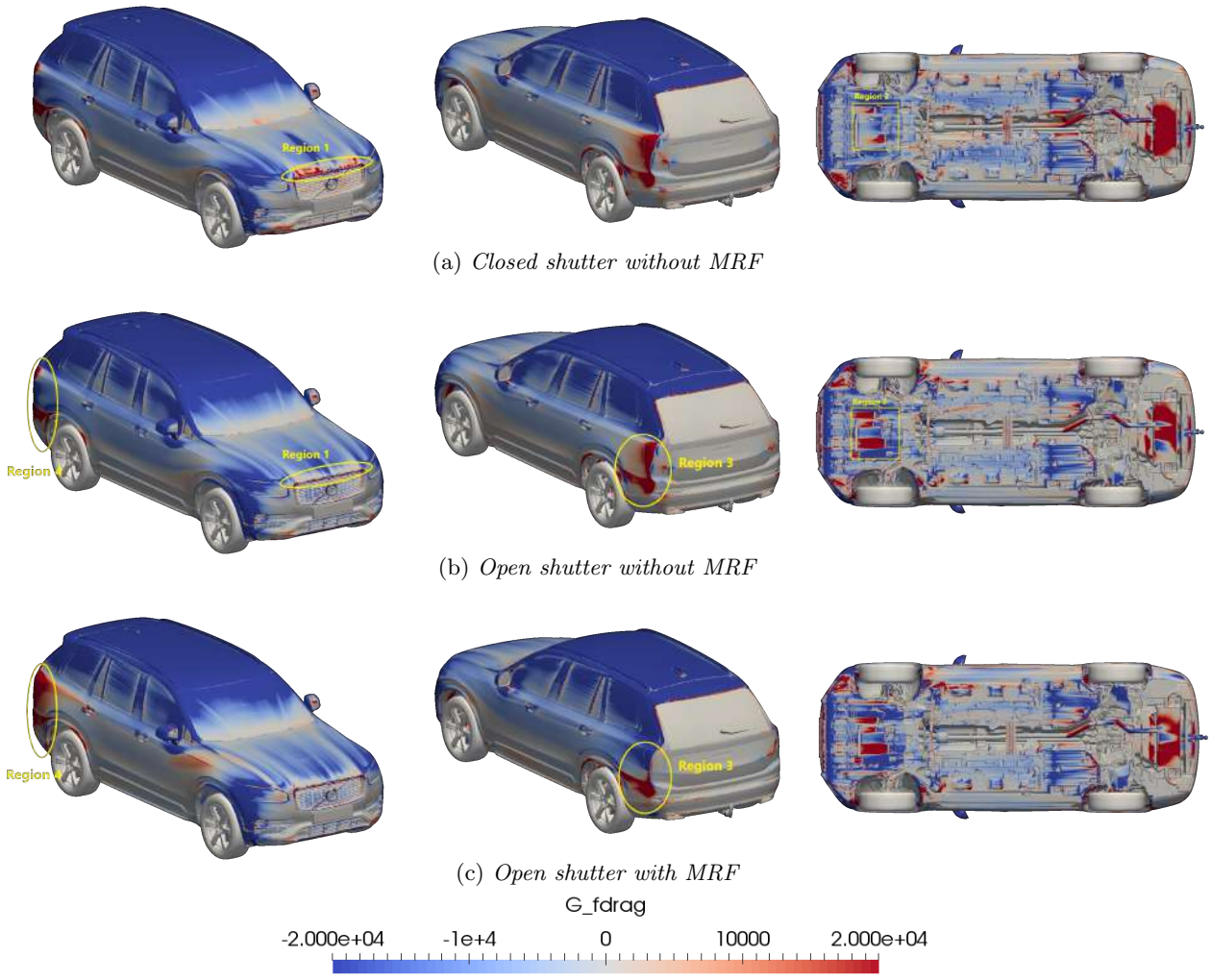

(a) *Closed shutter without MRF*

(b) *Open shutter without MRF*

(c) *Open shutter with MRF*

Figure 5.1: *DDES-based sensitivity maps for XC90 close shutter without MRF, open shutter with MRF and open shutter without MRF conditions*

The majority of adjoint prediction for close and open shutter conditions is similar, a pronounced difference occurs at the front-end and the bonnet (region 1), because the closed shutter blocks the air flow into engine bay, which impacts the flow in the vicinity of the shutter. For the closed shutter configuration, it can be seen that the flow detaches and the sensitivities imply that the curvature should be increased locally. For the rest exterior, the sensitivity map seems not very sensitive to the different shutter configurations. Both conditions predict an obvious red region on the rear sides, which implies moving this region outwards could result in a lower drag.

The sensitivities of the underbody for the close and the open shutter configurations are similar except the prediction in the vicinity of NACA duct, seen the region 2. Although the prediction of both cases indicates that the NACA duct region needs to move outwards, open shutter model has a larger red region compared with the closed one. The sensitivity field is similar in the rear, except for a small region on the rear muffler. This distinction is attributed to the different underbody air flows due to the contrary shutter configurations.

In addition, the difference of the drag factor between these two cases is also small, only five counts deviation. The MRF function applied in the wheel region influences the trajectory of the flow around the wheel house to some extent, which is the main reason for the diverse sensitivities on the rear side, seen the region 3 and the region 4. Overall, the effect of the MRF function on the sensitivities is limited, the sensitivities on the rest of the exterior and the underbody are almost same.

6 Conclusion and future work

6.1 Conclusion

A comprehensive investigation of RANS-based and DDES-based adjoint simulations for the DrivAer model has been conducted. It has been shown that both the RANS-based and the DDES-based adjoint predict similar sensitivity maps of drag minimisation for the majority of the exterior. The main difference is observed in regions where the flow has separated, where the DDES-based adjoint is preliminary considered to be more trust-worthy. The trends of the sensitivity maps prediction have been confirmed for selected regions for both the RANS-based and the DDES based adjoint simulations.

Although the sensitivity morphing in ANSA provides a smoothing process, this method is unable to generate an aesthetically pleasant surface. The noise in the sensitivity map combined with inappropriate morphing can easily lead to a worse geometry. The surface smoothness is of vital importance in geometry morphing. Alternatively, the direct morphing can be applied by defining morphing entities, control entities, translate vector and bounds. This approach allows for a large deformation and ensures a smooth surface.

Three configurations of the DrivAer model have been simulated, the notchback, the fastback and the squareback. The simulations were performed with RANS-based adjoint using Realizable k-ε turbulence model and DDES-based adjoint using Spalart-Allmaras turbulence model respectively, the same for the modified cases. The XC90 model is only evaluated by DDES-based adjoint simulation using Spalart-Allmaras turbulence model. The adjoint field tended to converge independent of the car types and simulation types.

6.2 Future work

Continuing work from here on should be to evaluate more critical regions to see if further improvements can be achieved. For example, the underbody can be a potential arena to reduce drag as well as the rear side regions. In addition, an effective optimisation procedure should be established to guide the designer in practice.

The results from the CFD simulations need to be verified by wind tunnel test to ensure the reliability of the results. Therefore, a wind tunnel test for using a full-scale model is needed to validate the accuracy of adjoint prediction.

Furthermore, the modification done to decrease drag often impact other aspects such as lift, which has a negative influence on the stability of the vehicle. To some extent, the drag-reduced modification would increase the rear lift, which has a negative influence on the stability of the vehicle. It would be interesting to combine these two aspects, i.e. drag and lift, and optimise them together as a combined objective.

References

[1] A. Jameson. Aerodynamic shape optimization using the adjoint method. *Lectures at the Von Karman Institute, Brussels* (2003).

[2] A. Jameson and S. Kim. Reduction of the adjoint gradient formula for aerodynamic shape optimization problems. *AIAA journal* **41**.11 (2003), 2114–2129.

[3] M. B. Giles and N. A. Pierce. An introduction to the adjoint approach to design. *Flow, turbulence and combustion* **65**.3-4 (2000), 393–415.

[4] B. Mohammadi and O. Pironneau. *Applied shape optimization for fluids*. Oxford University Press, 2010.

[5] R. Lohner, O. Soto, and C. Yang. "An adjoint-based design methodology for CFD optimization problems". *41st Aerospace Sciences Meeting and Exhibit*. 2003, p. 299.

[6] O. Soto and R. Lohner. On the computation of flow sensitivities from boundary integrals. *AIAA Paper* **112** (2004), 2004.

[7] C. Othmer. A continuous adjoint formulation for the computation of topological and surface sensitivities of ducted flows. *International Journal for Numerical Methods in Fluids* **58**.8 (2008), 861–877.

[8] C. Othmer. Adjoint methods for car aerodynamics. *Journal of Mathematics in Industry* **4**.1 (2014), 1–23.

[9] L. Davidson. Fluid mechanics, turbulent flow and turbulence modeling. *Chalmers University of Technology, Goteborg, Sweden (Nov 2011)* (2011).

[10] Spalart, Philippe R and Deck, Shur and Shur, ML and Squires, KD and Strelets, M Kh and Travin, A. A new version of detached-eddy simulation, resistant to ambiguous grid densities. *Theoretical and computational fluid dynamics* **20**.3 (2006), 181–195.

[11] T. Blacha and M. Islam. The Aerodynamic Development of the New Audi Q5. *SAE International Journal of Passenger Cars-Mechanical Systems* **10**.2017-01-1522 (2017).

[12] P. Spalart and S. Allmaras. "A one-equation turbulence model for aerodynamic flows". *30th aerospace sciences meeting and exhibit*. 1992, p. 439.

[13] Shih, T-H and Liou, WW and Shabbir, A and Yang, Zhigang and Zhu, Jiang. A new k-epsilon eddy viscosity model for high Reynolds number turbulent flows: Model development and validation (1994).

[14] Deck, Sébastien and Duveau, Philippe and d'Espiney, Paulo and Guillen, Philippe. Development and application of Spalart–Allmaras one equation turbulence model to three-dimensional supersonic complex configurations. *Aerospace Science and Technology* **6**.3 (2002), 171–183.

[15] Blacha, Thomas and Gregersen, Misha Marie and Islam, Moni and Bensler, Henry. *Application of the Adjoint Method for Vehicle Aerodynamic Optimization*. Tech. rep. SAE Technical Paper, 2016.

[16] A. I. Heft, T. Indinger, and N. A. Adams. *Introduction of a new realistic generic car model for aerodynamic investigations*. Tech. rep. SAE Technical Paper, 2012.

[17] C. J. Greenshields. Openfoam user guide. *OpenFOAM Foundation Ltd, version* **3**.1 (2015).

[18] Thomas, Schumacher and Carsten, Othmer and others. Adjoint optimization for vehicle external aerodynamics. *International Journal of Automotive Engineering* **7**.1 (2016), 1–7.

[19] C. Othmer, E. Papoutsis-Kiachagias, and K. Haliskos. "CFD optimization via sensitivity-based shape morphing". *Proceedings of the 4th ANSA & μETA Internat. Conf., Thessaloniki, Greece, BETA CAE Systems SA*. 2011.

[20] R. Yazdani. *Steady and Unsteady Numerical Analysis of the DrivAer Model*. 2017.

[21] S. Sebben. *Numerical simulations of a car underbody: effect of front-wheel deflectors*. Tech. rep. SAE Technical Paper, 2004.

[22] R. H. Barnard. *Road vehicle aerodynamic design-an introduction*. 2009.

[23] R. P. Dwight and J. Brezillon. Effect of approximations of the discrete adjoint on gradient-based optimization. *AIAA journal* **44**.12 (2006), 3022–3031.

[24] Ashton, N and West, A and Lardeau, S and Revell, A. Assessment of RANS and DES methods for realistic automotive models. *Computers & Fluids* **128** (2016), 1–15.

A Appendix

A.1 Probe location

The probe location refers to the following figure, the probe 3, 4 locate on the underbody.

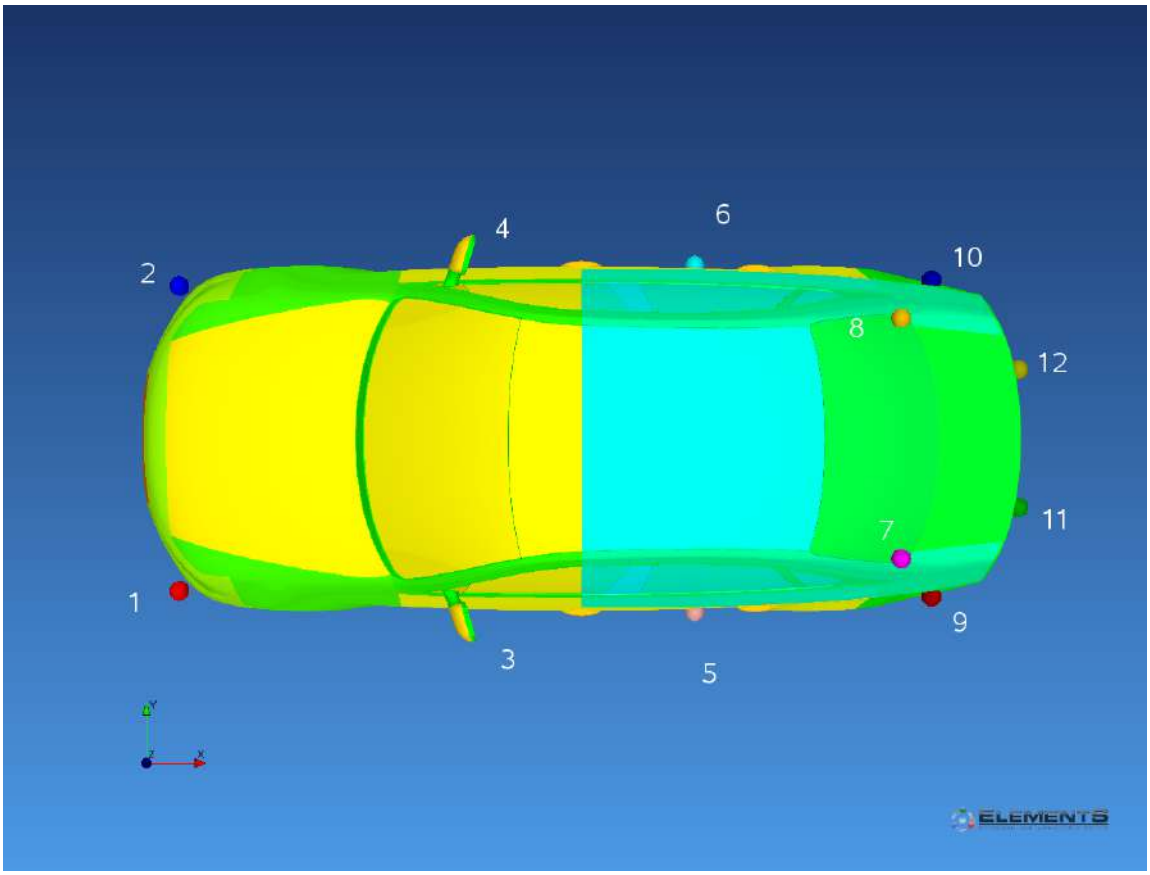

Figure A.1: *Probe locations*

A.2 Sensitivity evolution for fastback

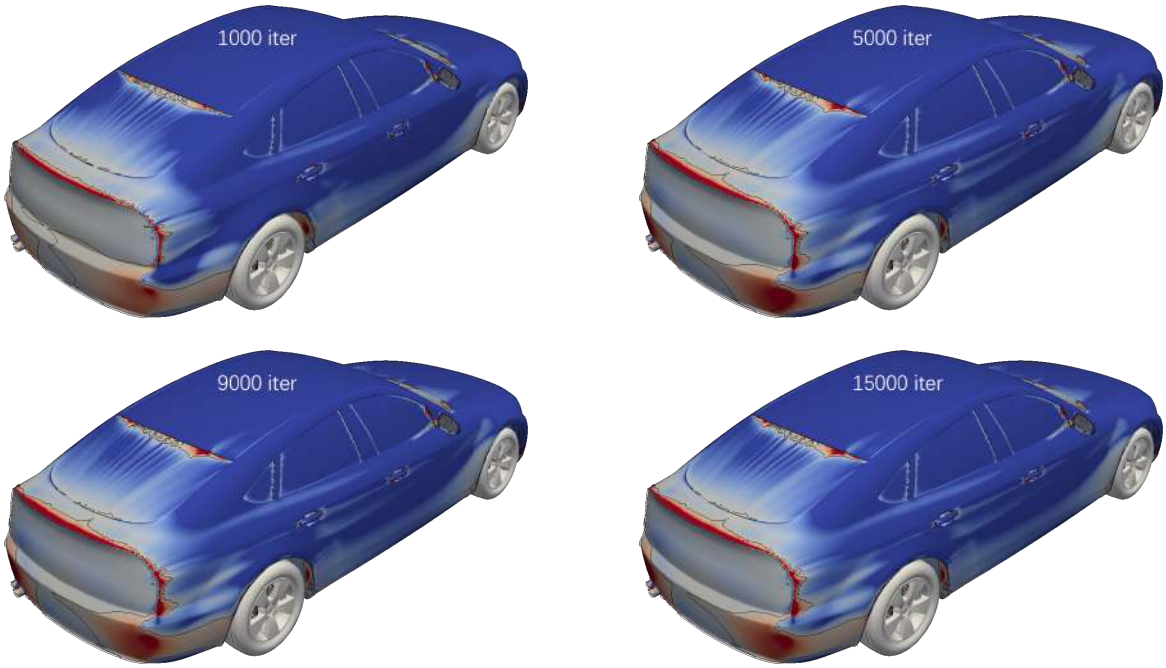

Figure A.2: *Evolution of sensitivity map for RANS-based adjoint in fastback configuration*

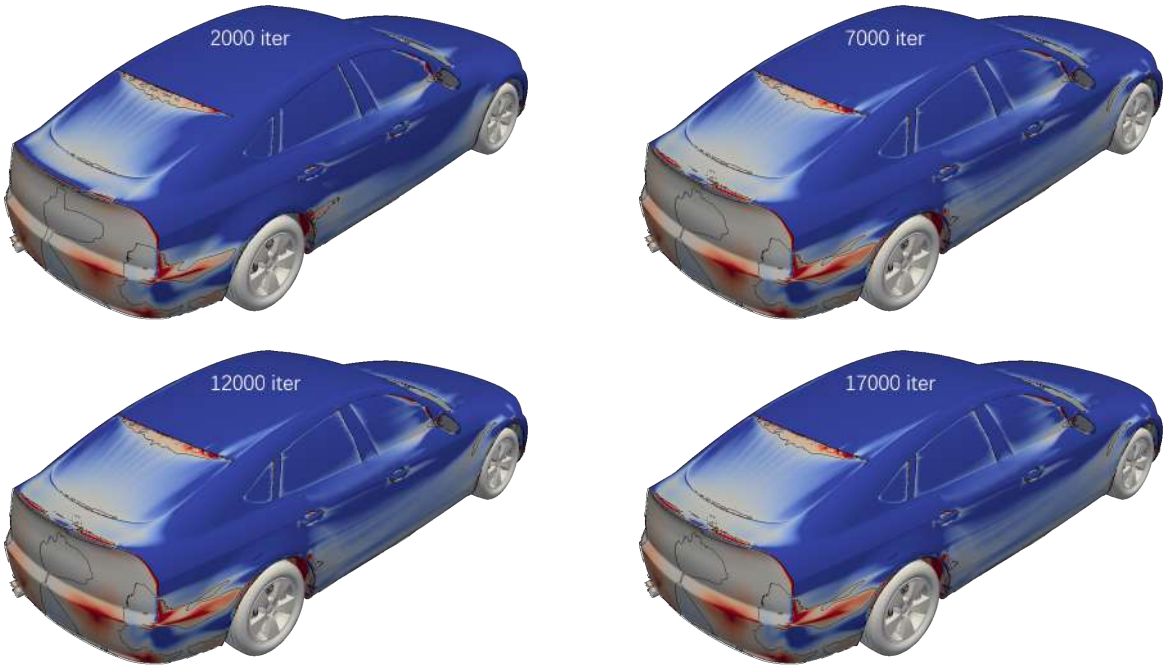

Figure A.3: *Evolution of sensitivity map for DDES-based adjoint in fastback configuration*

A.3 Sensitivity evolution for squareback

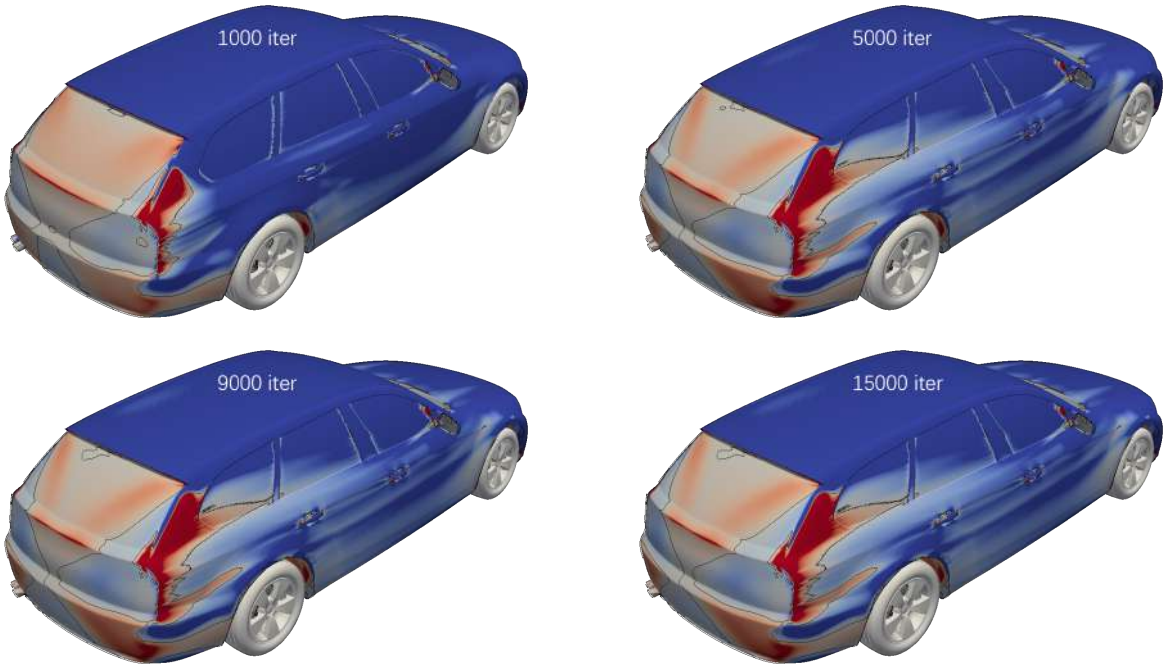

Figure A.4: *Evolution of sensitivity map for RANS-based adjoint in squareback configuration*

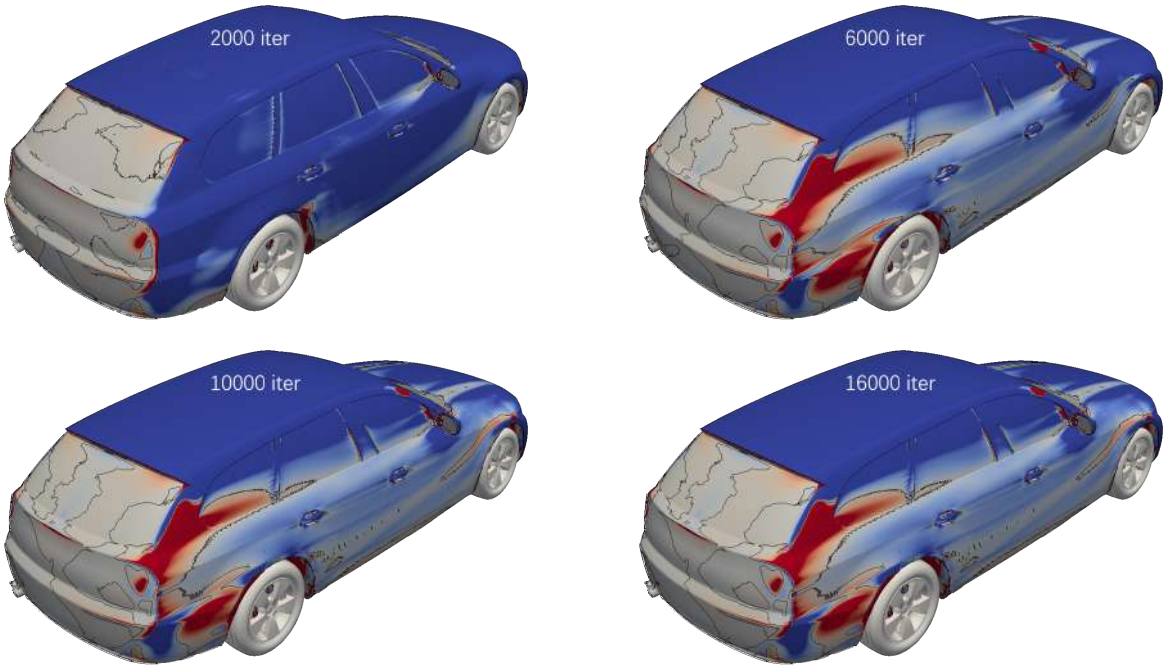

Figure A.5: *Evolution of sensitivity map for DDES-based adjoint in squareback configuration*